



TECHNICAL UNIVERSITY MUNICH

DEPARTMENT OF PHYSICS



Max-Planck-Institut für Physik

MAX PLANCK INSTITUTE FOR PHYSICS  
WERNER HEISENBERG INSTITUTE

Master's Thesis in Nuclear, Particle and Astrophysics

---

**Modelling of the Tritium  $\beta$ -Decay  
Spectrum for Sterile Neutrino  
Search with KATRIN and Analysis  
of the First Tritium Data**

---

Author: Madlen Steven

Supervisor: Prof. Dr. Susanne Mertens



# 1 Erklärung

Hiermit versichere ich die Arbeit selbstständig verfasst und keine anderen als die angegebenen Quellen und Hilfsmittel benutzt zu haben sowie alle dem Wortlaut oder Sinn nach entnommenen Inhalte anderer Werke an den entsprechenden Stellen unter Angabe der Quelle kenntlich gemacht zu haben.

Madlen Steven  
München, Dezember 2018



## 2 Abstract

The Karlsruhe Tritium Neutrino (KATRIN) experiment is designed to improve the  $\nu$ -mass sensitivity to about  $0.2 \text{ eV}/c^2$  (90% C.L.) by measuring the shape of the endpoint of the tritium  $\beta$ -decay spectrum. By extending the measurement interval to the whole spectrum it will also be possible to search for so called sterile neutrinos. This hypothetical fourth neutrino flavour eigenstate does not interact via the weak, strong and electromagnetic force. A corresponding mass eigenstate of order keV could be observed as a kink in the  $\beta$ -decay spectrum. As the current modelling software of the KATRIN experiment considers only the endpoint of the tritium spectrum, it has to be extended for sterile neutrino search. In this thesis the basic idea of this new simulation software is presented with the focus on detector-related effects. Moreover the first data taken with KATRIN is analysed regarding sterile neutrino search and a first exclusion limit on the sterile neutrino parameters is given.



# Contents

<b>1</b>	<b>Erklärung</b>	<b>i</b>
<b>2</b>	<b>Abstract</b>	<b>iii</b>
<b>3</b>	<b>Neutrino Physics</b>	<b>1</b>
3.1	Discovery of the Neutrino . . . . .	1
3.1.1	Experimental Set-Up . . . . .	1
3.1.2	Detection of $\nu_\mu$ and $\nu_\tau$ . . . . .	4
3.2	Active Neutrino Mass . . . . .	6
3.2.1	First Evidence for Neutrino Oscillations . . . . .	6
3.3	Discovery of Neutrino Oscillations . . . . .	7
3.3.1	Oscillation Parameters . . . . .	8
3.4	Sterile Neutrinos . . . . .	9
3.4.1	Possible Types of Sterile Neutrinos . . . . .	9
<b>4</b>	<b>The KATRIN Experiment</b>	<b>12</b>
4.1	Imprint of the $\nu$ mass on the $\beta$ -Decay Spectrum . . . . .	12
4.2	Measurement Principle . . . . .	15
4.3	Experiment Set-up . . . . .	15
4.3.1	Rear Section . . . . .	15
4.3.2	Source Section . . . . .	15
4.3.3	Windowless Gaseous Tritium Source . . . . .	16
4.3.4	Transport Section . . . . .	16
4.3.5	Differential Pumping Section . . . . .	17
4.3.6	Spectrometer Section . . . . .	18
4.3.7	Detector . . . . .	21
4.4	Response Function . . . . .	23
<b>5</b>	<b>The TRISTAN Project</b>	<b>25</b>
5.1	Phase 0 . . . . .	26
5.2	Phase 1 . . . . .	27
<b>6</b>	<b>Simulating Particles with Kassiopeia</b>	<b>28</b>
6.1	Electromagnetic Field Computation . . . . .	29
6.2	Particle Tracking . . . . .	31
6.3	Particle Interactions . . . . .	32
<b>7</b>	<b>Simulation Software: SSC-Sterile</b>	<b>34</b>
7.1	Requirement of New Simulation Software for Sterile Neutrino Search . . . . .	34
7.2	Modelling the Tritium Beta Decay Spectrum with SSC-sterile . . . . .	36
7.3	Modelling of the Detector Response . . . . .	39
7.3.1	Simulation Settings . . . . .	39
7.3.2	Results . . . . .	41
7.4	Retarding Potential Dependence . . . . .	42
7.4.1	Simulation Settings . . . . .	42

7.4.2	Results	42
<b>8</b>	<b>Analysis of First Tritium Data for Sterile Neutrino Search</b>	<b>47</b>
8.1	First Tritium Campaign	47
8.2	Configuration for First Tritium Measurements	47
8.3	Physics Model	48
8.3.1	Spectrum and Response	48
8.3.2	Detection Efficiency	50
8.4	Analysis Strategy	51
8.4.1	Selection and Combination of Pixels and Runs	52
8.5	Statistical Method	52
8.6	Treatment of Systematics	52
8.6.1	Including Systematics with the Covariance Matrix	53
8.7	MC-Generation	54
8.8	Results from Real Data	56
8.8.1	qU-scans	58
8.8.2	Comparison to Exclusion Lines from Other Runs	61
8.8.3	Results from Other Experiments	62
<b>9</b>	<b>Conclusion and Outlook</b>	<b>63</b>
	<b>References</b>	<b>67</b>

## 3 Neutrino Physics

In the Standard Model there are three types of neutrinos: electron, muon and tau neutrino. They are spin one-half, uncharged fermions and thus do not participate in the electromagnetic and strong interaction. Although they are assumed to be massless in the Standard Model it has been shown that neutrinos change their flavour while propagating [1, 2]. This is known as the phenomena of neutrino oscillations and shows that neutrinos actually do have a mass. This discovery was awarded with the Nobel prize in 2015. In this chapter an overview of the history and theory of neutrino physics will be given.

### 3.1 Discovery of the Neutrino

In the first theories of the  $\beta$ -decay the neutron was assumed to decay into a proton and an electron which would constitute a two body decay. Thus without an additional particle the  $\beta$ -decay would lead to a discrete energy and momentum in the final state due to energy and momentum conservation. But in contradiction the spectrum was measured to be continuous (see figure 1). This would imply violation of energy conservation if it was a decay into two particles. The existence of another particle could solve this problem of energy violation as it carries away the missing energy.

In 1930 Wolfgang Pauli came up first with the idea of a new particle with spin  $\frac{1}{2}$ , the neutrino<sup>1</sup>. About two years later in 1934 Enrico Fermi developed his theory of the four-fermion interaction which can describe the  $\beta$ -decay theoretically [4]. This was before the theory of the weak interaction was developed. According to the weak interaction particles interact by exchanging massive bosons. In Fermi's theory the interaction of the four particles is reduced to one vertex (see figure 2) and thus it is an effective description of the weak interaction. The coupling constant on this vertex is described by the Fermi constant  $G_F$ . "Fermi's golden rule" then allows the calculation of the transition probability per unit of time of the  $\beta$ -decay via the first order of perturbation theory

$$\Gamma_{i \rightarrow f} = \frac{2\pi}{\hbar} \rho(E_f) |\langle f | H' | i \rangle|^2.$$

Here  $\rho(E_f)$  describes the density of the final states, and  $|\langle f | H' | i \rangle|$  is the matrix element which describes the transition of an initial state  $|i\rangle$  which is disturbed by a potential  $H'$  to the final state  $|f\rangle$ .

#### 3.1.1 Experimental Set-Up

After its postulation it took 20 years more to discover the neutrino or, more precisely, the antineutrino. This happened in 1956 with the Reines-Cowan experiment that made use of the inverse  $\beta$ -decay

$$\bar{\nu}_e + p \rightarrow e^+ + n$$

in which an electron anti-neutrino  $\bar{\nu}_e$  and a proton  $p$  are transformed into a positron  $e^+$  and a neutron.

---

<sup>1</sup>Originally Pauli called his particle "neutron" but when in 1932 James Chadwick discovered a neutral particle with the mass of a proton and named it "neutron" [3] Fermi renamed the particle to "neutrino" which can be translated as "little neutral one"

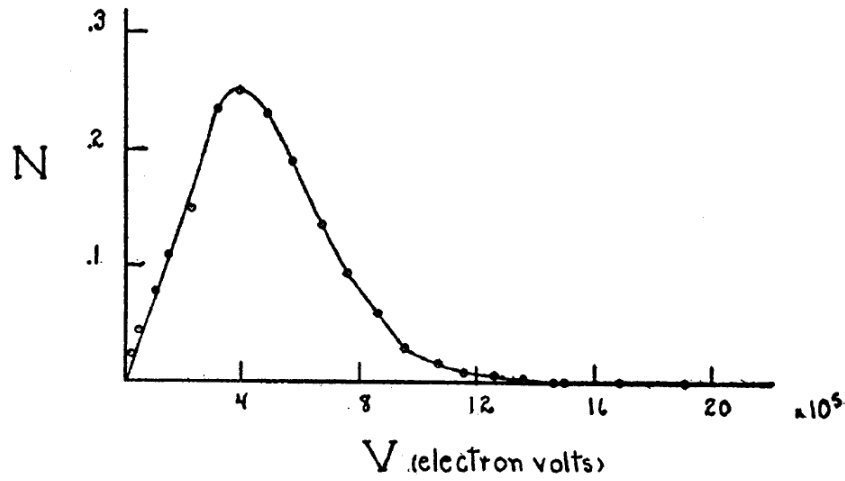


Figure 1: |  **$\beta$ -Decay Spectrum.**  $\beta$ -decay spectrum from radium. The spectrum is not discrete which would be the case for a two body decay but rather continuous [5].

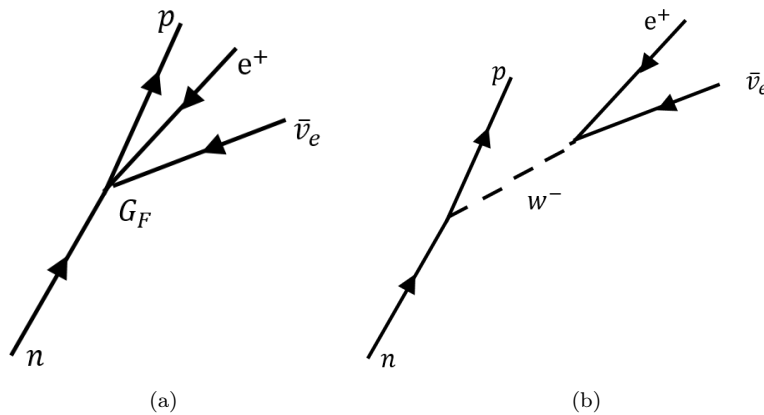


Figure 2: | **Feynman Diagram  $\beta$ -decay.** In Fermi's theory the interaction of four fermions is approximated to be point-like and thus occur only in one vertex. This would lead to the graph in a). In contrast, the weak interaction describes the interaction of weakly interacting particles by the exchange of massive bosons. According to the weak interaction the  $\beta$ -decay results in the graph in b). The four fermion approximation is valid only if all energies is small compared to the mass of the exchanged boson.

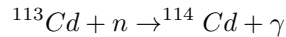
As the outgoing particles have a higher rest mass than the ingoing particles this process is only possible if the neutrino carries enough energy.

The probability of a neutrino to interact with a detector material is very low. Therefore a source with a high neutrino flux as well as a large detector was required to be able to detect neutrinos. A nuclear reactor near the detector could comply this requirement. The original idea was to only detect the positron that was created in the decay. This positron would interact with an electron in the detector material creating two photons with energies of two times the electron mass

$$e^+ + e^- \rightarrow \gamma + \gamma$$

The gammas created then by the annihilation of electron and positron would induce ionization cascades with ultraviolet photons that excite the scintillation material. The scintillation material in turn emits visible light that can then reach photomultiplier tubes as the scintillation material is transparent to visible light and thus can be detected.

But detecting only the annihilation photons would have led to high background rates that would have made the detection of the neutrino impossible. To reduce this background and be able to distinguish neutrino signals from background signals not only the positron but also the  $\beta$ -decay neutron was finally detected. As cadmium is a good neutron absorber it was added to the scintillator in order to capture the neutron. After capturing the neutron the cadmium nucleus emits a photon



which can then be detected (see figure 3 ). Due to the moderation the time it takes for neutron to be absorbed is typically some micro seconds higher than the immediate signal from the positron. This leads to a very “heartbeat” signal that made it possible to separate neutrinos from background signals.

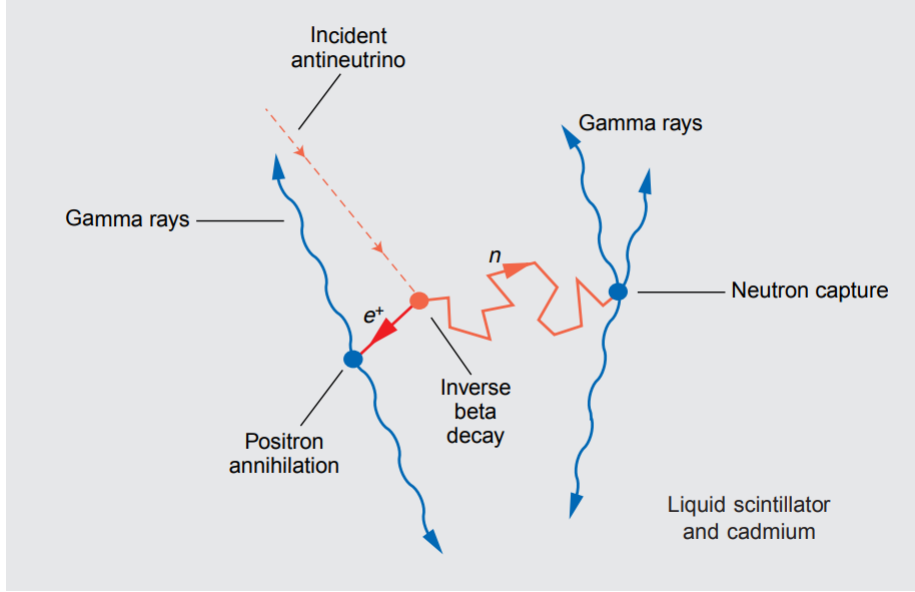


Figure 3: | **Detection Principle Anti-Neutrino.** The final detection principle consists of the coincident signals of the gammas created by the annihilation of the electron and positron and the gamma rays created by the de-excitation of the cadmium nucleus that had captured the neutron from the inverse  $\beta$ -decay. Picture from [6].

After the Hanford experiment did not succeed due to neutrino like signals from cosmic rays, Reines and Cowan started a second trial with the Savannah River experiment. The final set-up of the experiment can be seen in figure 4. It consists of a sandwich configuration with two layers of large tanks filled with 200 liter of water that contained dissolved cadmium chloride and three layers of liquid scintillators. An inverse  $\beta$ -decay in one of the cadmium-water tanks could induce only signals in the neighbouring layers as the photons would be too low energetic to hit the third detector. In contrast, cosmic particles events would be uncorrelated and thus lead to random signals. After being improved the Savannah River Experiment was finally able to directly detect the electron anti-neutrino.

### 3.1.2 Detection of $\nu_\mu$ and $\nu_\tau$

In 1962 the  $\nu_\mu$  was found by Leon Lederman, Melvin Schwartz and Jack Steinberger at the Brookhaven National Laboratory. This time an accelerator was used to produce the neutrinos by shooting protons on Beryllium targets to produce pions and kaons. The pions and kaons then decay to muons and muon anti-neutrinos. To shield the muons, the beam was guided first to a wall consisting of steel that let only the neutrinos pass as they do hardly interact. This results into a pure neutrino beam that exits the wall. After passing the steel wall the beam encountered an Aluminium spark chamber. An electron neutrino would have led to a particle shower but what was

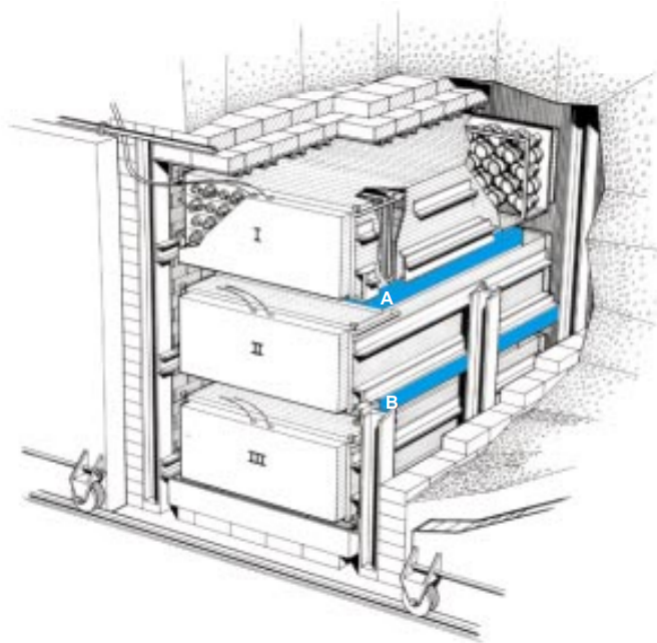


Figure 4: | **The Savannah River Experiment.** The Savannah River Experiment was able to detect the electron neutrino. To distinguish neutrino events from cosmic ray background the detector was set up with different layers of alternating scintillation and water-cadmium layer. Picture from [6].

measured in the spark chamber were straight tracks and thus it could be concluded that there had to be a second flavour of neutrinos, the muon neutrinos [7].

The tau neutrino was discovered even later in the year 2000 by the DONUT collaboration. They made use of the reaction

$$\nu_\tau + n \rightarrow \tau + p. \quad (1)$$

Tau neutrinos were created from decaying D-mesons that were in turn produced by the collision of Tungsten with protons accelerated by the Tevatron at Fermilab. Again other particles were shielded such that only the tau neutrinos could enter the emulsion target where the tau leptons were produced via equation 1. Due to the short half life of the tau lepton  $\tau_{\frac{1}{2},\tau} = 3.609 \times 10^{-13} \text{ s}$  they leave a short track in the emulsion before they decay again and thus leave a characteristic kink signal and can be distinguished from other neutrino flavours. Although the cross section of the reaction is very low and they were able to only detect four tau neutrinos this was enough for the discovery of the so far last neutrino flavour [8].

## 3.2 Active Neutrino Mass

Although in the Standard Model neutrinos are assumed to be massless, the discovery of the neutrino oscillations has this shown not to be true. The parameters of the oscillation depend on the squared mass difference of the neutrinos' mass eigenstates. Therefore non-zero square mass differences will lead to at least two non-zero neutrino masses.

### 3.2.1 First Evidence for Neutrino Oscillations

The first evidence for neutrino oscillations were made by the Homestake experiment in the 1960s, constructed under the direction of Raymond Davis [9]. The experiment aimed to measure solar neutrino flux to confirm theories and calculations on the Solar Model. The experiment was set up in the Homestake Gold Mine near South Dakota and used a radiochemical detection technique and 600 tons of tetrachloroethylene to detect neutrinos via the inverse  $\beta$ -decay

$$\nu_e + {}^{37}\text{Cl} \rightarrow {}^{37}\text{Ar} + e. \quad (2)$$

First neutrinos were captured via equation 2 and later the Argon can be extracted from the Chlorine and be counted and thus determine the number of detected neutrinos.

Surprisingly the number of measured neutrinos reached just a third of the expectations. This was named "solar neutrino problem".

### PMNS matrix

In order to explain the missing electron neutrinos coming from the sun and solve the solar neutrino a formalism was needed to explain the disappearance. For this reason the Pontecorvo–Maki–Nakagawa–Sakata (PMNS) matrix  $U$  was in analogy to the CKM matrix in the strong interaction, introduced as

$$\begin{bmatrix} \nu_e \\ \nu_\mu \\ \nu_\tau \end{bmatrix} = \begin{bmatrix} U_{e1} & U_{e2} & U_{e3} \\ U_{\mu1} & U_{\mu2} & U_{\mu3} \\ U_{\tau1} & U_{\tau2} & U_{\tau3} \end{bmatrix} \begin{bmatrix} \nu_1 \\ \nu_2 \\ \nu_3 \end{bmatrix} \quad (3)$$

The neutrino wave functions can be expressed in two different bases. This implies two different sets of eigenstates: the flavour eigenstates and the mass eigenstates. The flavour eigenstates are the eigenstates that participate in the weak interaction and couple to the W and Z bosons whereas the mass or energy eigenstates propagate through space and time. The two sets of eigenstates are connected by the PMNS matrix displayed in equation 3. By definition the flavour eigenstates do not have a defined mass as well as the mass eigenstates do not have a defined flavour. They are just a superposition of the respective eigenstates.

As the PMNS matrix is three dimensional this leads to three mixing angles  $\theta_{ij}$  which can be seen by decomposing the PMNS matrix into the three rotations in the eigenstate space:

$$U = \begin{bmatrix} 1 & 0 & 0 \\ 0 & \cos(\theta_{23}) & \sin(\theta_{23}) \\ 0 & -\sin(\theta_{23}) & \cos(\theta_{23}) \end{bmatrix} \cdot \begin{bmatrix} \cos(\theta_{13}) & 0 & \sin(\theta_{13}) \cdot e^{-i\delta} \\ 0 & 1 & 0 \\ -\sin(\theta_{13}) \cdot e^{i\delta} & 0 & \cos(\theta_{13}) \end{bmatrix} \cdot \begin{bmatrix} \cos(\theta_{12}) & \sin(\theta_{12}) & 0 \\ -\sin(\theta_{12}) & \cos(\theta_{12}) & 0 \\ 0 & 0 & 1 \end{bmatrix},$$

where  $\delta$  denotes the CP violating phase<sup>2</sup> and  $\theta_{ij}$  the rotation angles.

The matrix elements enable the calculation of the time evolution and the oscillation probability which yields for the case electron to muon neutrino oscillation in vacuum in first approximation

$$P(\nu_e \rightarrow \nu_\mu) = \sin^2(2\theta_{13}) \cdot \sin^2(\theta_{23}) \cdot \sin^2\left(\frac{\Delta m_{12}^2 L}{4E}\right).$$

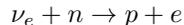
Therefore the oscillation angles influence the amplitude of the oscillations whereas the mass square difference  $\Delta m_{ij}^2 \equiv m_i^2 - m_j^2$  as well as the ratio of the total energy and the oscillation length  $\frac{E}{L}$  define the oscillation frequency. As the function is symmetric with respect to the argument of the last sine the oscillation of neutrinos in vacuum can give no insight into the sign of the mass difference and neither the absolute mass scale of the neutrinos.

### 3.3 Discovery of Neutrino Oscillations

Several experiments followed the Homestake experiment and among these the SNO experiment in Canada. The SNO detector is located 2 km below the surface of the earth in order to shield cosmic radiation and consists of a spherical tank filled with 1000 tons of  $D_2O$ . The experiment was divided into two phases

- **Phase 1**

In the first phase of the experiment the tank was filled with nothing more than  $D_2O$ . Electron neutrinos would interact with the neutron inside the deuterium to create an electron via



For solar neutrinos this charged current process is only possible for electron neutrinos as a muon neutrino would require to produce a muon due to the conservation of lepton number but the solar neutrinos do not carry enough energy to be able to produce a muon.

The created electron on the other hand has enough energy to generate Cherenkov light which can be then detected with photomultipliers.

---

<sup>2</sup>CP symmetry denotes the invariance of a state under charge and parity conjugation.

- **Phase 2**

In the second phase sodium chloride was added to the deuterium and enables also the neutral current process of dissolving the deuterium into neutron and proton. As this process has a much lower energy threshold all of the three neutrino flavours can be measured.

The comparison of both phases showed that the missing electron neutrinos events could instead be detected as muon and tau neutrinos. This means that the neutrinos indeed changed their flavour on the way from the sun to the Earth and therefore this proves right the hypothesis of neutrino oscillations.

### 3.3.1 Oscillation Parameters

As the neutrino oscillation was proven right what was missing were the parameters arising from the introduction of mass eigenstates. The parameters to be determined are the three mixing angles, two mass differences and the CP violating phase. Assuming a framework of  $3 \times 3$  neutrino eigenstates the oscillation parameters have been measured by various experiments. The results are listed in table 1.

Table 1: | **Oscillation Parameters.** The best-fit values for the oscillation parameters from [10]. The values without brackets correspond to the normal hierarchy, the values with brackets to the inverted hierarchy.

Parameter	best-fit	$3\sigma$
$\Delta m_{21}^2 [10^{-5} \text{ eV}^2]$	7.37	6.93 – 7.96
$\Delta m_{31(23)}^2 [10^{-3} \text{ eV}^2]$	2.56 (2.54)	2.45 – 2.69 (2.42 – 2.66)
$\sin^2 \theta_{12}$	0.297	0.250 – 0.354
$\sin^2 \theta_{23}, \Delta m_{31(32)}^2 > 0$	0.425	0.381 – 0.615
$\sin^2 \theta_{23}, \Delta m_{32(31)}^2 < 0$	0.589	0.384 – 0.636
$\sin^2 \theta_{13}, \Delta m_{31(32)}^2 > 0$	0.0215	0.0190 – 0.0240
$\sin^2 \theta_{13}, \Delta m_{32(31)}^2 < 0$	0.0216	0.0190 – 0.0242
$\delta/\pi$	1.38 (1.31)	$2\sigma$ : (1.0 - 1.9) ( $2\sigma$ : (0.92-1.88))

As mentioned already the oscillations in vacuum will not give any information about the sign of the mass difference. Nevertheless the sign of  $\Delta m_{12}^2$  was determined to be negative [10] which was possible due to matter effects that change the oscillation probability when the neutrinos are passing the sun. The sign of  $\Delta m_{23}^2$  on the contrary is still unknown and lead to two possible scenarios which are the normal hierarchy which is the case if  $m_3 > m_2 > m_1$  and the inverted hierarchy that refers to the case  $m_2 > m_1 > m_3$ .

A third possibility could be the case that the masses are degenerated such that the mass differences are very small compared to the actual masses which would lead to  $m_1 \approx m_2 \approx m_3$ .

### 3.4 Sterile Neutrinos

A sterile neutrino is considered a neutrino that does not interact weakly. A natural way to introduce this sterile neutrino would be to postulate a right-handed neutrino which would by construction be sterile as only left-handed fermions interact weakly. This is an intuitive way of introducing a sterile neutrino because all fermions in the Standard Model except the neutrinos occur with left-handed chirality as well as with right-handed chirality. So why should the neutrinos be the only particles in the Standard Model only appearing left-handed?

Sterile neutrinos would be introduced in the framework by extending the PMNS matrix by at least one dimension to:

$$\begin{pmatrix} \nu_e \\ \nu_\mu \\ \nu_\tau \\ \nu_s \end{pmatrix} = \begin{pmatrix} U_{e1} & U_{e2} & U_{e3} & U_{e4} \\ U_{\mu1} & U_{\mu2} & U_{\mu3} & U_{\mu4} \\ U_{\tau1} & U_{\tau2} & U_{\tau3} & U_{\tau4} \\ U_{s1} & U_{s2} & U_{s3} & U_{s4} \end{pmatrix} \begin{pmatrix} \nu_1 \\ \nu_2 \\ \nu_3 \\ \nu_4 \end{pmatrix} \quad (4)$$

An additional flavour eigenstate would come with a fourth mass eigenstate  $\nu_4$  as well as an additional active-sterile mixing angle  $\theta_s$ . As no sterile neutrino has been detected so far the mixing has to be very small and thus the overlap of sterile neutrino and the fourth neutrino mass eigenstate has to be large. Therefore sometimes the new mass is considered “sterile neutrino mass”. Technically speaking the sterile neutrino has no defined mass as it is a flavour eigenstate.

#### 3.4.1 Possible Types of Sterile Neutrinos

This thesis focuses on sterile neutrinos with masses in the keV-range, but there are more possibilities:

- **eV Sterile Neutrino**

The main motivation for eV sterile neutrinos comes from measurements made by the short baseline oscillation experiments which measured an anomaly in the rate of reactor anti-neutrinos [11]. This *reactor anti-neutrino anomaly* could be explained by introducing a light sterile neutrino[12]. Accordingly the missing anti-neutrinos could have changed their flavour and have oscillated to eV sterile neutrinos.

However eV sterile neutrinos are ruled out to be dark matter: Due to the small mass they would constitute **Hot Dark Matter** (HDM). Hot dark matter refers to dark matter with energies large compared to their mass. Hot dark matter is disfavoured due to the observations from the formation of galaxy clusters. The results from observing structure formation indicate a scenario in which at first galaxies were formed that then grouped together in galaxy clusters (bottom-up scenario). In contrast to that hot dark matter would wash out small scale structures. Structure formation would in the beginning only be possible for large scale structures such as galaxy clusters which later decompose into galaxies (top-down scenario).

- **$\gg$  GeV Sterile Neutrino**

The masses of the neutrinos are very small compared to the masses of other massive particles in the Standard Model. The Yukawa couplings to the Higgs boson would have to be unreasonably

small to explain the lightness of the neutrinos. One advantage of a right handed heavy sterile neutrino would be that it could give an explanation on the smallness of the neutrino mass: There are two ways to include a mass term in the Lagrangian. The first would be via a Dirac mass term [13]

$$\mathcal{L}_D = \frac{1}{2}m_D(\bar{\nu}_L\nu_R + \bar{\nu}_L^C\nu_R^C) + H.c.$$

with the Dirac mass  $m_D$  and the left- ( $L$ ) and right-handed ( $R$ ) (anti)neutrinos fields  $(\bar{\nu})\nu$ . The superscript  $c$  indicated the charge conjugation. The first term in the Dirac term for example would destroy a right-handed particle and create a left-handed particle [14].

The second possibility is via a Majorana mass term

$$\mathcal{L}_M = \frac{1}{2}m_L\bar{\nu}_L\nu_R^C + \frac{1}{2}m_R\bar{\nu}_L^C\nu_R + H.c.$$

The Majorana term would violate the electric charge conservation and is therefore forbidden for quarks and charged leptons but as neutrinos do not carry electric charge they would be immune to this violation and this Majorana term would also be possible in the Lagrangian. Combining the two mass terms leads to [15]

$$\begin{aligned}\mathcal{L}_{D+M} &= \frac{1}{2}m_D(\bar{\nu}_L\nu_R + \bar{\nu}_L^C\nu_R^C) + \frac{1}{2}m_L\bar{\nu}_L\nu_R^C + \frac{1}{2}m_R\bar{\nu}_L^C\nu_R + H.c. \\ &= \frac{1}{2}(\bar{\nu}_L, \bar{\nu}_L^C) \begin{pmatrix} m_L & m_D \\ m_D & m_R \end{pmatrix} \begin{pmatrix} \nu_R^C \\ \nu_R \end{pmatrix} + H.c.\end{aligned}$$

The physical values that would be measured are however the eigenvalues of the mass matrix. After some calculation one arrives at the eigenvalues

$$m_{1,2} = \frac{1}{2} \left[ m_L + m_R \pm \sqrt{(m_L - m_R)^2 + 4m_D^2} \right]$$

Assuming a right-handed neutrino mass  $m_R$  which is much larger than the Dirac mass  $m_D$

$$m_R \gg m_D$$

as well as a vanishing left-handed neutrino mass  $m_L = 0$  this simplifies the mass eigenvalues to

$$m_\nu \approx \frac{m_D^2}{m_R} \qquad m_N \approx m_R$$

The larger  $m_R$  the smaller is the neutrino mass due to the inverse proportionality. This effect is called "seesaw-effect". A large right-handed neutrino mass would therefore lead to a very tiny physical neutrino mass and therefore avoid the problem with the tiny Yukawa coupling very elegantly.

- **keV Sterile Neutrino**

A keV sterile neutrino could be **Warm Dark Matter** (WDM) and could mitigate the tensions that appear in **Cold Dark Matter** (CDM) models [16].

It would give an imprint on the energy spectrum of a  $\beta$ -decay as long as the mass of its corresponding eigenstate is below the endpoint of the spectrum. As KATRIN can measure the tritium spectrum with high precision it is not only sensitive to the active neutrino mass but also to sterile neutrinos. So the TRISTAN project which is part of the KATRIN experiment was brought to life with the aim to search for sterile neutrinos. In section 5 the TRISTAN Project will be described in more detail.

## 4 The KATRIN Experiment

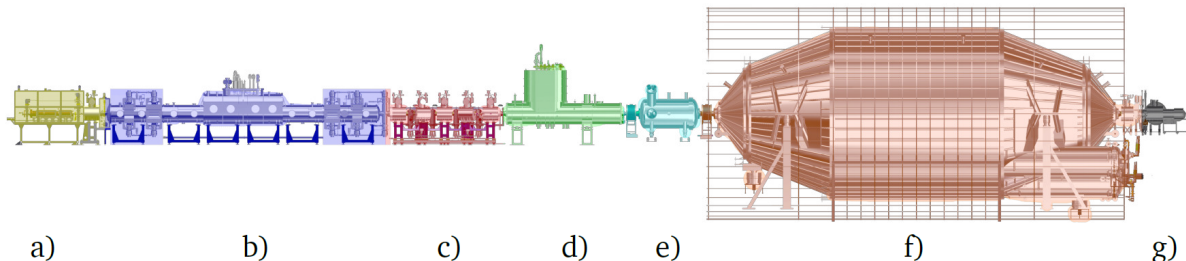


Figure 5: | **Set-Up KATRIN Experiment.** The figure shows the set-up of the KATRIN experiment. The electrons are created in the decay of tritium atoms in the **Windowless Gaseous Tritium Source (WGTS)** (b). After passing the WGTS in forward direction they arrive at the differential (c) and cryogenic pumping section (d). Here the tritium gas molecules are separated from the electrons letting only the latter reach the pre-spectrometer (e) and main spectrometer section (f). The spectrometers define the lower energy cut-off on the spectrum that depends on the voltage applied to the vessels. Finally the electrons are led to the detector section (g) where they deposit energy and can be measured. Electrons moving towards the backward direction arrive at the rear wall (a). Figure from [17].

Oscillation experiments have shown that neutrinos are massive particles and determined most of the parameters defining the oscillations: the three mixing angles, the two mass differences and at least one mass difference sign.

What still remains unknown is the absolute scale of the neutrino masses as it does not influence the neutrino oscillations. This means that a different approach for tracking down the neutrino mass is needed. One of the several complementary approaches to do so is the measurement principle used in the KATRIN experiment that is located at the **Karlsruhe Institute of Technology (KIT)** in Karlsruhe.

### 4.1 Imprint of the $\nu$ mass on the $\beta$ -Decay Spectrum

The **KARlsruhe TRITium Neutrino (KATRIN)** Experiment aims to determine the scale of the active neutrino mass with a sensitivity of  $0.2 \text{ eV}/c^2$  at 90% confidence level (C.L.) [18] which corresponds to a discovery of a neutrino mass of  $0.35 \text{ eV}$  at  $5\sigma$  after a net measurement time of three years.. This improves the current best limits from the experiments in Mainz [19] and Troitsk [20, 21], that measured the neutrino mass to be [10]

$$m_\beta < 2.3 \text{ eV}/c^2 \text{ at } 95\% \text{ C.L. (Mainz)} \quad m_\beta < 2.05 \text{ eV}/c^2 \text{ at } 95\% \text{ C.L. (Troitsk)} .$$

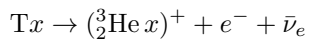
The neutrino mass  $m_\beta$  is an effective mass that is defined by

$$m_\beta = \sqrt{\sum_{i=1}^3 |U_{ei}^2| m_{\nu i}}$$

The resolution of the KATRIN experiment is not good enough to resolve the tiny mass differences of the mass eigenstates. Instead they melt to an effective mass eigenstate. Accordingly the masses  $m_i$  of the mass eigenstates are weighted with the matrix elements  $U_{ei}$  of the PMNS matrix.

The KATRIN experiment performs a direct, model-independent measurement of the neutrino mass. The signature of a non-vanishing neutrino mass will be a different spectrum shape in the endpoint region of the tritium  $\beta$ -decay compared to a spectrum with vanishing neutrino mass. The endpoint thereby refers to the maximal energy an electron released in the  $\beta$ -decay can have assuming  $m_\beta = 0$ .

KATRIN does not use atomic but molecular tritium. Therefore the tritium  $\beta$ -decays will occur in a molecule that consists of a tritium atom that is bounded to another Hydrogen isotope. This makes the following decays possible



where  $x$  is one of T, D or H. Each of the decays has a slightly different spectrum due to different **Final State Distributions (FSD)**: As the  $\beta$ -decay takes place in tritium molecules, this gives rise to rovibrational<sup>3</sup> states as well as electronic excited states. If the Tritium molecule is not in the ground state after the decay, this diminishes the maximal energy the electron can have.

The energy that gets released in a decay due to the different masses of initial and final particles, splits up into the kinetic energies of the decay products. The neutrino mass reduces the maximal amount of energy the electron can carry away. This will manifest in the endpoint region of the electron's energy spectrum as a slightly different shape. The KATRIN experiment will measure the endpoint region with high precision and thereby gain insight into the value of the neutrino mass. Mathematically the differential tritium spectrum can be described by

$$\frac{d\Gamma}{dE}(m_\beta) = C \cdot F(E, Z') p_e(E + m_e) \cdot \sum_j P_j (E - E_0 - X_j) \sqrt{(E - E_0 - X_j)^2 - m_\beta^2} \quad (5)$$

where  $C = G_F^3 \cos^2 \Theta_C |M_{nuc}^2| / (2\pi)^3$  is constant (with the Fermi coupling constant  $G_F$ , the Cabbibo angle  $\Theta_C$  and the nuclear matrix element  $M_{nuc}$ ),  $F(E, Z')$  is the Fermi function<sup>4</sup> for a daughter nucleus with atomic number  $Z'$  and an electron with energy  $E$ , the electron momentum  $p_e$  and mass  $m_e$  and the endpoint energy  $E_0$ . The sum runs over the excited states  $X_j$  that are weighted with their respective probability  $P_j$ .

---

<sup>3</sup>rotational and vibrational

<sup>4</sup>The Fermi function accounts for the interaction of outgoing  $e^-$  with the nucleus.

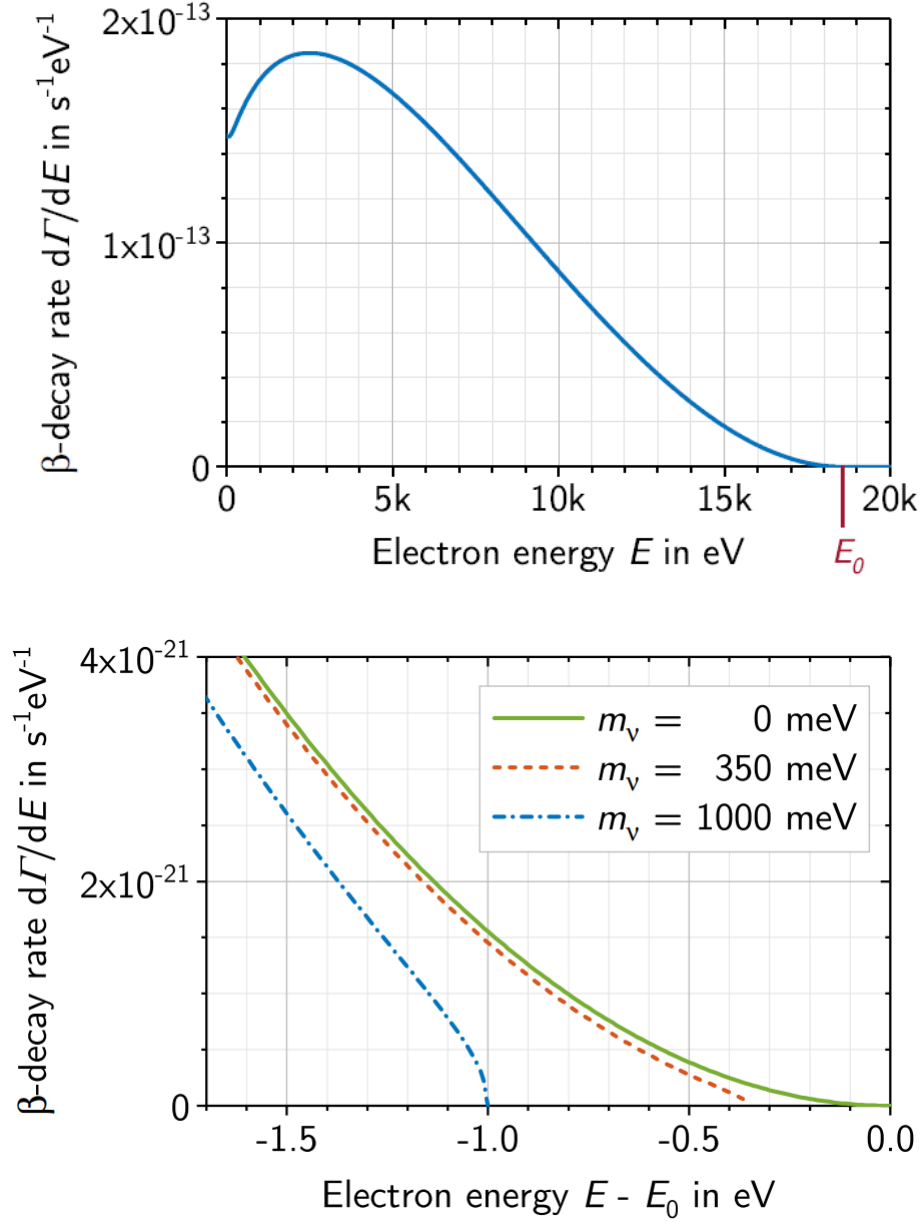


Figure 6: | **The  $\beta$ -Decay Spectrum.** The imprint of the neutrino mass on the  $\beta$ -decay spectrum will be the shape in the endpoint region. A non-vanishing neutrino mass will change the shape of the energy spectrum as well as the position of the endpoint compared to an energy spectrum without massive neutrinos. Figure from [22].

## 4.2 Measurement Principle

The measurement will be performed as an integral measurement: This means that what will be measured, is the electron rate counted in the detector depending on an retarding potential that is applied to the main spectrometer. The energy of the incoming electrons is underpart, that what matters most is only the number. The spectrum is scanned in a way that the the count rate at distinct retarding potentials in the spectrometer is measured. The neutrino mass reduces the amount of incoming electrons in the endpoint region compared to a spectrum with massless neutrinos.

## 4.3 Experiment Set-up

Obtaining the design sensitivity sets several conditions on the KATRIN set-up. In the following the main components as introduced in [18] are described in more detail.

### 4.3.1 Rear Section

The Rear Section confines the Source in the backward direction. It consists of two components which are the differential pumping section DPS2-R and the Calibration and Monitoring System (CMS). The DPS2-R has two pumping ports that guide the tritium into the outer loop (the loop system is briefly described below) from where it can be re-injected into the source. It is separated to the CMS by a gate valve V2-R.

A rear plate in the CMS makes sure that the electric potential is maintained throughout the full **W**indowless **G**aseous **T**ritium **S**ource (WGTS). Moreover the CMS provides an electron gun as well as an electron detector that are necessary for monitoring the flux of the  $\beta$ -decay electrons.

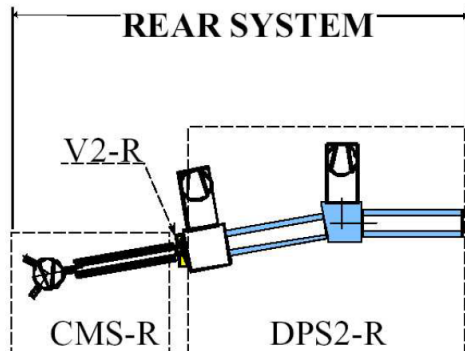


Figure 7: | **Rear Section.** The Rear Section consists of a differential pumping section and a Calibration and Monitoring System [23].

### 4.3.2 Source Section

The neutrino mass has an impact on the spectrum of every  $\beta$ -decaying element. So theoretically any of them could be used for the neutrino mass measurement. Finally the radioactive isotope tritium was chosen because the following reasons:

- The molecular structure of Tritium is relatively simple. This makes it possible to obtain theoretical results on their the FSD.
- Tritium has an endpoint of about  $E_0 = 18.6$  keV. This is rather low compared to other nuclei and advantageous as the relative number of electrons with energies near the endpoint increases for smaller endpoints ( $\sim E_0^{-3}$ ). Because this region contains the information of the neutrino mass high statistics and therefore a small endpoint is desired [13].

- Tritium has a half-life time of  $t_{1/2} = 12.3$  y. This is reasonably short and thus provides a high statistic with at low gas density.

The **Tritium Laboratory Karlsruhe** (TLK) was founded in the beginning of the 90s and is hosted by the KIT. It has the license to handle up to 40 grams of tritium and hence was elected to supply the KATRIN experiment with tritium.

### 4.3.3 Windowless Gaseous Tritium Source

The **Windowless Gaseous Tritium Source** (WGTS) is a tube of 10 m length to which the gaseous molecular tritium is injected. Instead of constraining the tube with windows to keep the tritium in the source, a loop system is used that pumps out the tritium and re-injects the collected tritium in the source. The loop system consists of an inner and an outer loop. The inner loop that filters 99% of the gas, contains a permeator letting only hydrogen isotopes pass and re-injects the tritium directly into the source. The remaining 1% of the gas is purified to tritium in the outer loop

system before entering the source once again. This is done to maintain the high tritium concentration in the source of at least 95% [25]. The KATRIN experiment performs an integral measurement and thus counts the electrons hitting the detector. The rate of the electrons reaching the detector depends on the composition of the source. Therefore the monitoring of the tritium composition is of utmost importance.

### 4.3.4 Transport Section

After leaving the WGTS and before passing the main spectrometer the electrons are guided through the transport system.

To prevent background due to tritium and maintain the ultra high vacuum in the spectrometer, the tritium flow has to be reduced by 14 orders of magnitude [18].

To make sure that only electrons and not tritium atoms can reach the spectrometers a transport system is required that holds back tritium but lets electrons pass. This transport system is divided into the Differential Pumping Section and the Cryogenic Pumping Section:

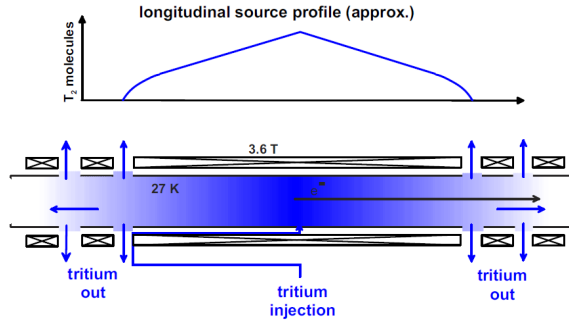


Figure 8: | **WGTS**. Windowless Gaseous Tritium Source. Figure from [24].

### 4.3.5 Differential Pumping Section

Because there is no wall between the WGTS and the main spectrometer, the reduction of the tritium is realized by a turbo pumping system. The first stage of the differential pumping section (DPS1) is situated at both ends of the WGTS. In the transport section the second forward differential pumping section (DPS2-F) is located. Originally it was designed to reduce the tritium flow by a factor of  $R = 10^5$  but due to the extension of the beam tube diameter, only a value of  $R = 2.5 \cdot 10^4$  could be reached [26].

The five DPS2-F beam tubes are tilted towards each other by  $20^\circ$  as can be seen in figure 9. Each of the tubes has a length of 1070 mm and an inner diameter of 81 mm-86 mm and is cooled down to 77 K. Between each of the five tube elements a pumping port (so four in total) with a throughput of  $2000 \frac{l}{s}$  is installed. The chicane-like structure of the beam tubes is chosen to prevent the neutral tritium molecules from entering the main spectrometer. On the other hand charged particles are guided adiabatically through the chicane structure. The magnetic fields, that are needed to guide the ions, are created by super-conducting magnets with magnetic field strength of 5.6 T.

As the positive charged ions are not blocked by the chicane itself they would be guided with the electrons to the main spectrometer. In order to absorb the positive ions, an additional electric field is applied [27]. While a magnetic field alone would only lead to a gyration, the electric field induces an additional drift ( $\vec{E} \times \vec{B}$ ) to the trajectories that is independent from the particle's properties. The light and fast electrons can pass rapidly the tubes whereas the heavy and slow tritium ions are exposed longer time to the electric field. They drift out of the flux tube and get absorbed.

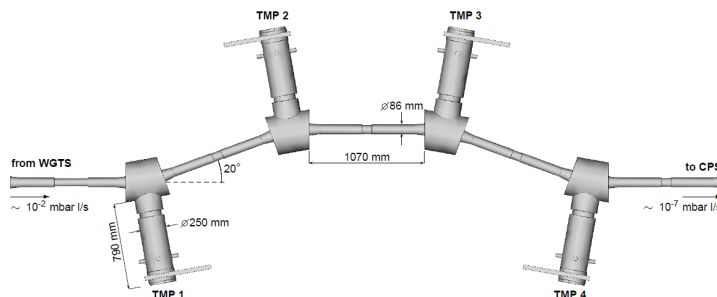


Figure 9: | **DPS**. Differential pumping system in the transport section. Picture from [26].

### Cryogenic Pumping Section

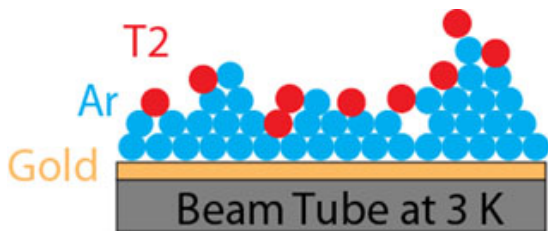


Figure 10: | **CPS**. Cryogenic pumping section. Figure from [24].

to 3 K and imposed on the inner surface of the beam tube elements. The tritium molecules stick

To reduce the tritium flow by another seven orders of magnitude another pumping section, the cryogenic pumping section (CPS), is set up behind the DPS. Similar to the DPS, it builds a chicane this time consisting of seven beam tubes that are tilted toward each other by  $15^\circ$ . The adiabatic transport of the electrons is achieved by super-conducting magnets that create magnetic fields of 5.6 T as before. The CPS does not include a pumping system but works with cryo-sorption. To enable a further reduction, the tritium is absorbed by argon cooled down

to the argon layer as can be seen in figure 9. Over time the argon layer saturates with the tritium condensate making absorption less effective. After an operation time of three month when about 1% of the argon layer are covered, it has to be regenerated<sup>5</sup> to maintain the effectiveness of the cryo-sorption [28]. Further information on the CPS can be found in [29].

### 4.3.6 Spectrometer Section

To be able to improve the current limits on the neutrino mass, the KATRIN experiment needs a very good energy resolution. This energy resolution depends on the MAC-E (**M**agnetic **A**diabatic **C**ollimation combined with an **E**lectrostatic) filter. Before going through this high precision filter in the main spectrometer the electrons have to pass the pre-spectrometer. This is a small version of the main spectrometer and reduces the electron flux by letting only high energy electrons in the important endpoint region pass. To do so, the pre-spectrometer as well as the main spectrometer are on high voltage to reflect low energy electrons.

#### MAC-E filter

An illustration of the working principle of the MAC-E filter can be seen in figure 12. The total kinetic energy  $E_{kin}$  of the electrons can be divided into a parallel  $E_{\parallel}$  and a orthogonal component  $E_{\perp}$ :

$$E_{kin} = E_{\parallel} + E_{\perp}$$

The retarding potential acts only on the energy component that is parallel to the applied potential. To be able to achieve the required energy resolution, the energy from the circular motion has to be transferred to the longitudinal motion. This is done by decreasing the magnetic field by many orders of magnitude. If the transfer happens adiabatically the magnetic field does not change the total momentum of the electron but only transfers one energy component to another. The condition for the transformation to be adiabatic is that the change of the magnetic field is small compared to the magnetic field  $B$

$$\frac{\Delta B}{B} \ll 1$$

within one cyclotron length  $l_c$

$$l_c = \frac{2\pi\gamma m_e v_{\parallel}}{Be}$$

where  $\gamma$  is the relativistic factor,  $m_e$  the electron mass,  $v_{\parallel}$  the velocity parallel to the magnetic field lines and  $e$  the electron charge.

The resolution of the MAC-E filter is then defined by the maximal  $B_{max}$  and minimal  $B_{min}$  magnetic field via

$$\frac{\Delta E}{E_e} = \frac{B_{min}}{B_{max}}$$

---

<sup>5</sup>In order to regenerate the layer and remove the tritium the temperature has to be increased until the tritium becomes gaseous and can evaporate.

Although electrons might carry enough energy to overcome the retarding potential they can nevertheless be reflected by the magnetic mirror. The maximal angle  $\theta_{max}$  of electrons that can pass the magnetic field without being reflected is given by

$$\sin(\theta_{max}) = \sqrt{\left(\frac{B_S}{B_{max}}\right)}$$

where  $B_{max}$  is the maximal magnetic field the electrons will see and  $B_S$  is the magnetic field at the starting position.



Figure 11: | **Main Spectrometer.** The main spectrometer of the KATRIN experiment. The left picture shows the arrival of the main spectrometer in Leopoldshafen. The spectrometer was build in Deggendorf which is only 220km distance away from Karlsruhe. But as the vessel is too large for a transport on the high way as well as passing the water gate of the Rhine–Main–Danube Canal, another route had to be found [30]. So instead, it was shipped down the Danube to the black See, through the Dardanelles, the Aegean Sea, the Bay of Biscay and the English Channel up to the Dutch coast. The right picture finally shows the main spectrometer installed in the Karlsruher Institute of Technology where it will be used to measure the mass of the neutrino. Both pictures are taken from [24].

## Principle of the MAC-E Filter

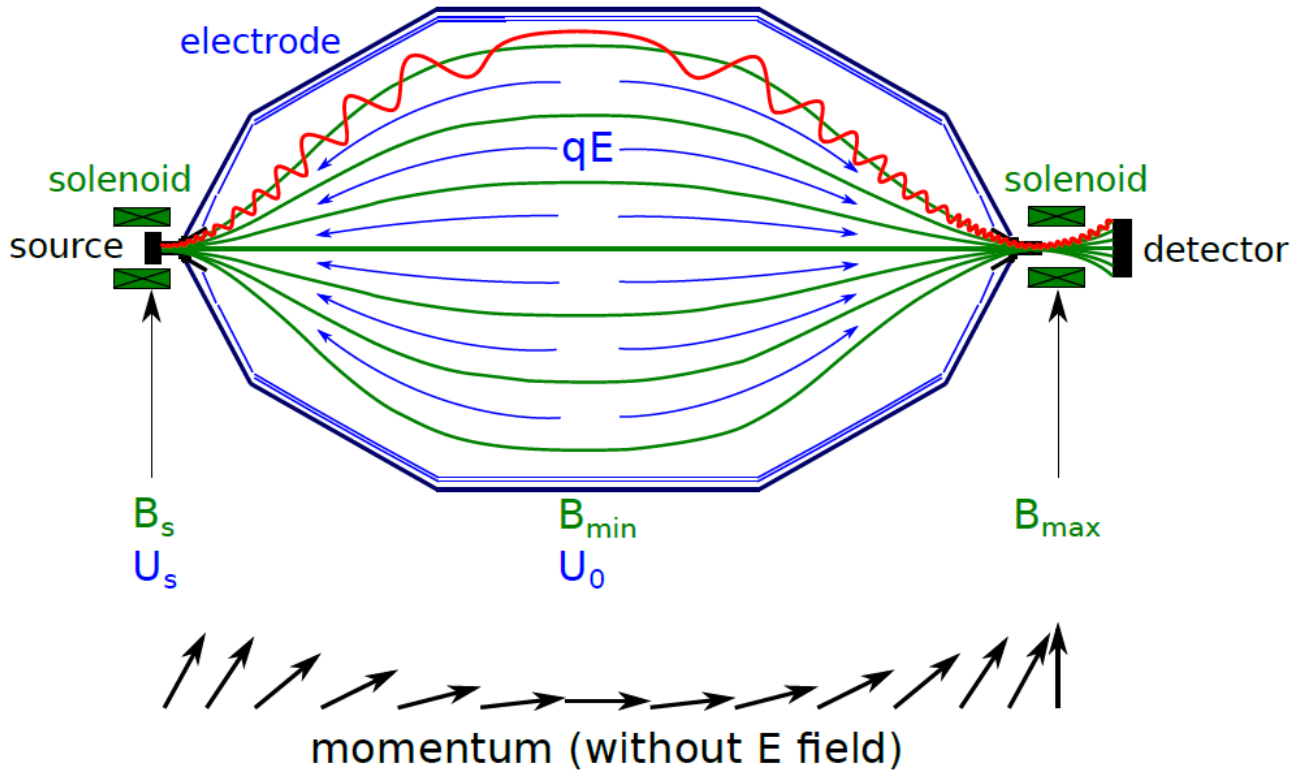


Figure 12: | **Principle of MAC-E Filter.** The figure illustrates the principle of the MAC-E filter as used in KATRIN. The electrons from the tritium  $\beta$ -decay are emitted in all directions and consequently have momenta that are not parallel to the electric field lines of the retarding potential. But as the retarding potential acts only on the energy component parallel to the field lines and not on the total energy, the part of the kinetic energy that is contained in the cyclotron motion has to be transformed into longitudinal motion. This is possible due to a large difference of 4 orders of magnitude of the magnetic fields in the source and the analysing plane. The analysing plane is located in the middle of the spectrometer. After the energy transfer the retarding potential finally can act on the total kinetic energy and reach a high energy resolution. After passing the main spectrometer the high energetic electrons are re-accelerated and counted in the detector. Figure from [31].

### 4.3.7 Detector

The neutrino mass measurement consists of an integral measurement. This means that in principle it would be sufficient only counting incoming electrons without further information on their energy. But nevertheless the detector, called **Focal Plane Detector (FPD)**, used in KATRIN is a 148-pixel silicon semiconductor detector with a 3 keV energy resolution. This enables the separation of tritium electrons and background: the tritium electrons only arrive the detector in a narrow energy window whereas background occurs on a larger scale of energy.

The 148 pixels are aligned in a circular shape and have in total a diameter of 9 cm. Each of the pixels is designed to detect the same fraction of flux tube. The pixels are divided into 13 rings where the most inner ring has four pixels and the rest of the rings consist of 12 pixels, each with an energy resolutions of 2-3 keV [33]. However this is only the resolution of the detector, the sensitivity on the neutrino mass is defined by the main spectrometer.

Not all of the energy that is deposited in the detector can also be detected. A part of the detector is not sensitive which means that in this part energy cannot be detected. This part is called “dead layer”<sup>6</sup>.

The influence of the dead layer has to be considered to be able to analyse the data properly.

<sup>6</sup>At the surface semiconductors have a “dead” layer that correspond to the doped regions which define the semiconductor’s properties [34]. If particles deposit energy in this layers, it cannot be collected completely.

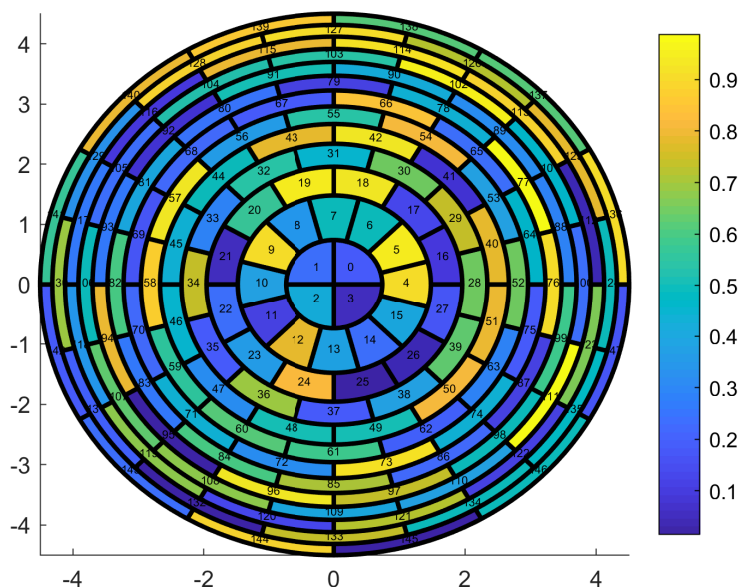
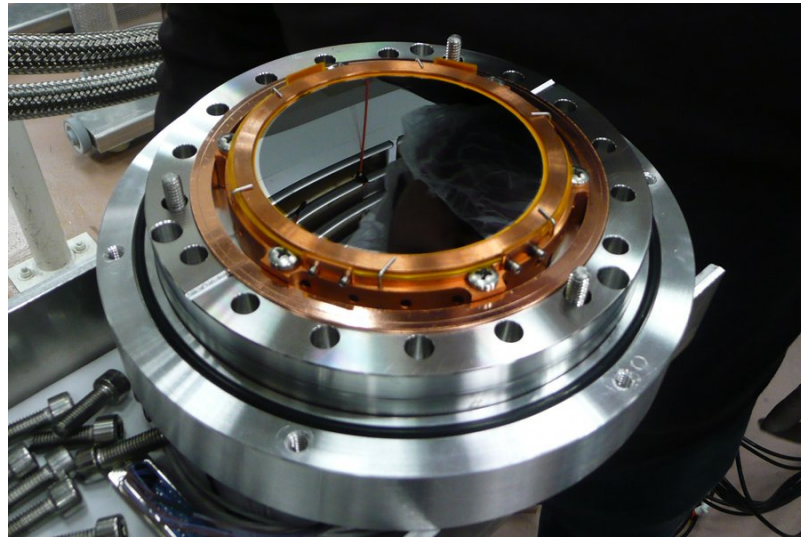


Figure 13: | **Focal Plane Detector**. The figure shows the arrangement of the 148 pixels in 13 rings. Figure from [32]

Figure 14: | **KATRIN Pixel Detector.** Picture of the silicon semiconductor detector that is used in KATRIN for the neutrino mass measurement. The detector does not only count the electrons but also provides an energy resolution to discriminate background events. Picture from [24].



## 4.4 Response Function

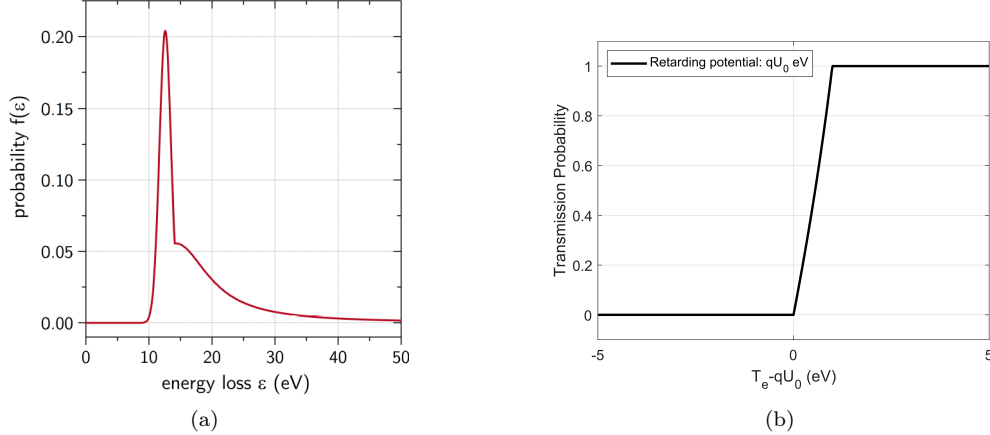


Figure 15: | **KATRIN Response Function.** The initial  $\beta$ -decay spectrum gets transformed in the KATRIN set-up on the way to the detector because electrons lose energy when scatter or do not even reach the detector because of getting reflected. The transformation of the initial spectrum is described by the response function. The figure on the left shows the typical energy loss of electrons scattering once. This empirical function is based on measurements from [35, 36]. The (discrete) energy peak in the spectrum results from excitation processes, the continuous part describes the energy loss due to ionization of tritium molecules. To describe multiple scatterings in the source the electron loss function is convolved with itself. The figure on the right shows the transmission function which is determined by the main spectrometer in the case of nominal settings. It can be calculated analytically for an isotropically emitting source. Pictures from [37].

The energy spectrum measured by the detector is not the theoretical  $\beta$ -spectrum as described by formula 5. The spectrum changes due to scatterings in the source, and the reflection of electrons in the main spectrometer or due to magnetic fields. As the pressure decreases outside the source, scatterings that occur in the transport section are negligible and not taken into account for the energy loss function. The transformation of the initial spectrum is described by the response function.

The rate of electrons reaching the detector depends on their initial energy  $E$  and the retarding potential in the main spectrometer  $U$ . Assuming an isotropically emitting source, the transmission function can be derived theoretically by integrating the differential transmission function

$$\mathcal{T}(E, U, \theta) = \begin{cases} 1 & \text{if } E \left(1 - \sin^2 \theta \cdot \frac{B_A}{B_S} \cdot \frac{\gamma+1}{2}\right) - qU > 0 \\ 0 & \text{else} \end{cases}$$

and is given by [22]:

$$\mathcal{T}(E, U) = \int_{\theta=0}^{\theta_{max}} \mathcal{T}(E, U, \theta) \sin \theta \, d\theta = \begin{cases} 0 & \text{if } E - qU < 0 \\ \frac{1 - \sqrt{1 - \frac{E - qU}{E} \frac{B_S}{B_A} \frac{2}{\gamma + 1}}}{1 - \sqrt{1 - \frac{B_S}{B_{max}}}} & \text{if } 0 \leq E - qU \leq \frac{B_A}{B_{max}} E \frac{\gamma + 1}{2} \\ 1 & \text{if } E - qU > \frac{B_A}{B_{max}} E \frac{\gamma + 1}{2} \end{cases} \quad (6)$$

with  $B_A$  the magnetic field in the analysing plane,  $B_S$  the magnetic field at the starting position,  $B_{max}$  the maximal magnetic field, the elementary charge  $q$  and the relativistic factor  $\gamma$ . The full response function includes, besides the transmission function, also additional transformations due to energy loss and scatterings in the source. The energy loss function as shown in figure 15 states how much energy an electron typically loses when scattering once. This energy loss depends on the particle's energy but as the mass measurement performed by KATRIN only considers the endpoint region (up to some tens of eV below the endpoint) the energy loss is considered as energy-independent. The spectrum consists of a discrete energy loss that is caused by the excitation processes and a continuous part from the ionization of tritium molecules. To be more specific the energy loss  $\epsilon$  is modelled by the empirical energy loss function

$$f(\epsilon) = \begin{cases} A_1 \cdot \exp\left(-2 \left(\frac{\epsilon - \epsilon_1}{\omega_1}\right)^2\right) & \text{if } \epsilon < \epsilon_c \\ A_2 \cdot \frac{\omega_2^2}{\omega_2^2 + 4(\epsilon - \epsilon_2)^2} & \text{if } \epsilon \geq \epsilon_c \end{cases}$$

where  $A_i$ ,  $\omega_i$  and  $\epsilon_2$  are the fit parameters that are optimized according to the measurements, the parameter  $\epsilon_1$  is fixed and the parameter  $\epsilon_c$  is chosen such that the two parts form a continuous function.

The response function is then obtained by integrating the differential response function

$$R(E, U) = \int_{\epsilon=0}^{E - qU} \int_{\theta=0}^{\theta_{max}} \mathcal{T}(E - \epsilon, \theta, U) \cdot \sin \theta \cdot \sum_s P_s f_s(\epsilon) \, d\theta \, d\epsilon$$

Here  $s$  specifies the number of scattering and  $f_s$  is the  $s$ -fold scattering. It is obtained by convolving the energy loss function for one scattering  $s$  times with itself and weighted by the probability  $P_s$  of the scattering to happen. The maximal angle  $\theta_{max}$  is restricted by magnetic reflection.

## 5 The TRISTAN Project

The **TR**itium **I**vestigation on **S**terile to **A**ctive Neutrino mixing (TRISTAN) is a subproject inside the KATRIN experiment that uses the KATRIN set-up to search for a sterile neutrino signature in the keV mass range accessible by the tritium  $\beta$ -decay.

The MAC-E filter is not able to resolve the tiny mass differences of  $\Delta m_{21}^2 = 7.37 \cdot 10^{-5} \cdot \text{eV}^2$  and  $\Delta m_{23}^2 = 2.56 \cdot 10^{-3} \text{eV}^2$  [10] of the active neutrinos and they are measured as the effective mass  $m_\beta$ . By assuming an additional mass eigenstate in the keV range, the now four mass eigenstates will no longer form one effective mass eigenstate but they can be resolved as two superposed spectra: the spectrum resulting from the effective mass defined by  $m_\beta^2 = \sum_{i=1}^3 |U_{ei}|^2 m_{\nu i}$  as before and the additional spectra resulting from the fourth mass eigenstate  $m_4$ . The final spectrum will consist of the superposition of these two decay spectra weighted according to the active to sterile mixing angle  $\theta_s$ :

$$\frac{d\Gamma}{dE} = \cos^2 \theta_s \frac{d\Gamma}{dE}(m_\beta) + \sin^2 \theta_s \frac{d\Gamma}{dE}(m_4) .$$

The superposition leads to a distortion and a kink in the  $\beta$ -decay spectrum as shown in figure 16.

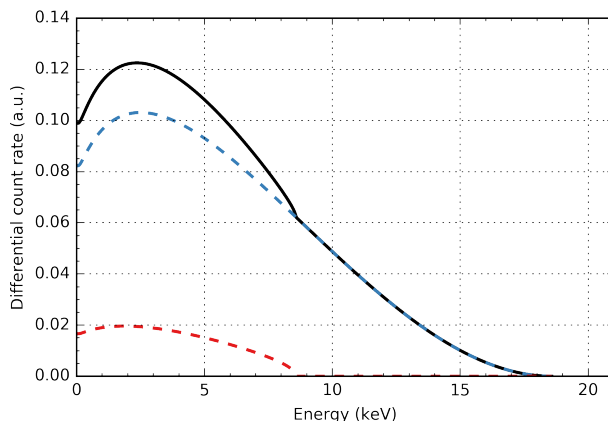


Figure 16: | **Tritium Spectrum with Sterile Neutrino.** The blue dashed line displays the  $\beta$ -spectrum weighted with  $\sin^2 \theta_S$ , the red dashed line displays the sterile neutrino spectrum with the endpoint  $E_0 - m_4/c^2 = 10$  keV weighted with  $\cos^2 \theta_S$  for a sterile mixing angle  $\sin^2 \theta_S = 0.2$ . A superposition of both spectra leads to the a kink in the spectrum (black line). Picture from [38].

This means that the signal TRISTAN is searching for would not be in the shape of the spectrum in the endpoint region but up to some keV deep in the spectrum. However, current KATRIN detector system is designed to measure low count rates in the endpoint region and cannot handle high electron fluxes. There are two ways to overcome this issue: One way would be the reduction of the tritium density. With less tritium the count rates far away from the endpoint will be low enough so that the detector system will be able to handle them. This will be “Phase 0” of the experiment. Another possibility is to measure with full intensity but to upgrade the detector so that is able to

measure the high signal rates that occur deep in the spectrum. This method will be used during “Phase 1”.

## 5.1 Phase 0

In Phase 0 the KATRIN set-up as it is used to search for a sterile neutrino signature. The measurement will be performed as an integral measurement. The readout system as well as the focal plane detector are only capable of handling up to  $10^5$  counts per second [39]. The source activity that is used for the neutrino mass measurement campaign is however four orders of magnitude higher. This requires a reduced signal count rate for sterile neutrino measurements. The reduction of the count rate is accomplished in two steps [40]:

- **Reduction of Gas Density**

The first step is to reduce the column density in the WGTS. This refers to the density of the gas inside the WGTS. It is the non-linear gas density integrated over the length of the tube [41] and it is given in units of molecules per area.

But the reduction of the tritium amount is limited: there is guarantee for the stability of the source for low gas densities.

- **Magnetic Field Configuration**

The second step is then to adjust the magnetic field configuration in order to increase magnetic reflection of electrons on their way to the detector: If a charged particle moves from a weaker into a stronger magnetic field its kinetic energy parallel to the magnetic field line gets transformed into the component perpendicular to the field lines. The particle gets decelerated up to the point where the direction of its momentum changes and the particle gets reflected [42]. This phenomenon is called magnetic mirror<sup>7</sup>. Whether or not the particle gets reflected depends on the starting angle  $\theta$ , the strength of the magnetic field at the starting point  $B_{start}$  and the maximal magnetic field  $B_{max}$ . Only particles with angles

$$\theta_{max} < \arcsin \sqrt{\frac{B_{start}}{B_{max}}}$$

can pass the maximal magnetic field.

Therefore an electron created with a large angle  $\theta$  in the source in a magnetic field  $B_{Start}$  cannot fulfil this equation and pass the magnetic field  $B_{max}$  to reach the detector. By adjusting the magnetic fields the count rate can be further reduced to ensure the required low count rates.

Both Phase 0 and the active neutrino mass measurement are performed as an integral measurement (see section 4.1) and therefore take advantage of the high energy resolution of the MAC-E filter.

---

<sup>7</sup>The reversed effect is used in the spectrometer. In contrast, the magnetic field is reduced and thus the particles are accelerated in the direction parallel to the magnetic field lines.

## 5.2 Phase 1

After having finished the neutrino mass measurement and Phase 0 of sterile neutrino search, the Phase 1 of sterile neutrino search will start to use the whole capacity of the WGTS to gain statistics faster. This requires a new detector capable of handling the high count rates occurring at energies far below the endpoint. The **Silicon Drift Detector (SDD)** that is used in this measuring phase is produced by the Halbleiterlabor of the Max-Planck-Society. To avoid a dead-area between the pixels they are constructed with a hexagonal pattern. The current prototypes consist of seven pixels and are produced with various diameters. The final TRISTAN detector will consist of 21 modules each consisting of 166 pixels. Each pixel has a diameter of about 3 mm resulting in a size of around 20 cm for the final detector.

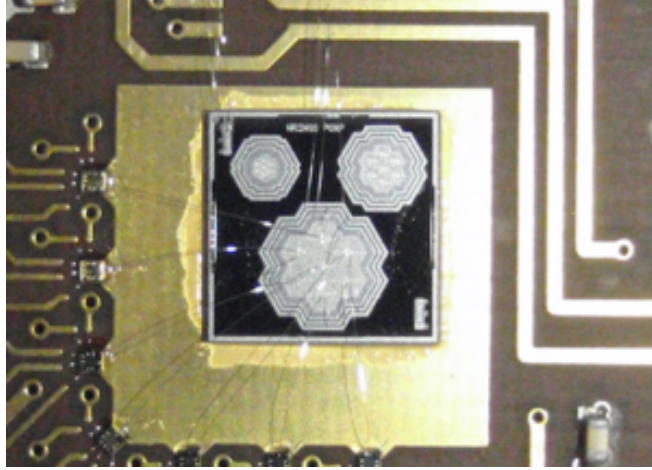


Figure 17: | **Prototypes of Pixel Detector for Phase 1 of the TRISTAN project.** The pixels are chosen to be hexagonal to avoid blind spots in the detector. Picture from [43].

The new detector is designed to fulfil the following criteria [39]:

- **High Rates**

To be able to handle the high electron rates the detector will have a large number of pixels ( $\sim 3500$ ). Moreover, it has to process the events fast which requires small shaping times ( $\leq \mu\text{s}$ ).

- **Energy Resolution**

In contrast to Phase 0, the measurement strategy is changed to a differential measurement for data taking in Phase 1. This is possible due to the high energy resolution of the new detector with **F**ull **W**idth **H**alf **M**aximum (FWHM) of 300 eV at 20 keV. Moreover, the detector is designed to have a small dead layer in the order of 10 nm.

- **Large Area Coverage**

The pixel diameter should not be smaller than 2 mm to diminish charge sharing from neighboring pixel [44].

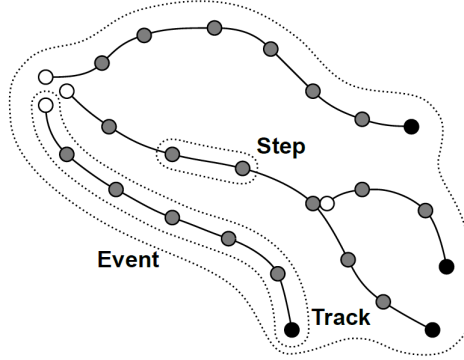


Figure 18: | **Terminology in KASSIOPEIA.** A run can be divided into events that consist of several tracks. Each track is split into steps which are the smallest unit in KASSIOPEIA simulations. Picture from [46].

## 6 Simulating Particles with Kassiopeia

The particle simulations for the KATRIN Experiment and thus the simulations used for this thesis are done with the C++ based KASSIOPEIA simulation package which is part of the KASPER package [45]. Besides the KASSIOPEIA package, KASPER also includes KGeoBag and KEMField that are of importance for the initialisation and description of the experiment set-up.

It includes the simulation of creating the particle, tracking in the experiment set-up considering the effects of the magnetic and electric fields on the particle and finally the detection of the particle in the detector. The simulation is performed event-by-event. There are four different levels of output which contain an output with a different amount of details.

- **step** A step is the most basic element that can be computed. It results from solving the equation of state. This calculation can be made either exactly and adiabatically<sup>8</sup>, as described below.
- **track** Several steps form a track and a determines the trajectory of a particle from its creation up to its termination. There are different cases that lead to the termination of the particle such as the crossing of a surface, a specific number of maximal steps or the crossing of a minimal or maximal coordinate that can be defined by the user.
- **event** In turn an event is formed by several tracks. The event consists of the whole trajectory of the initial particles and the possible secondary particles which may be created due to interactions. The number of events is defined in the configuration xml-file.
- **run** The highest level in the hierarchy is the run. A run is the simulation of all the events. Multiple runs can be realised by merging runs with the same set-up.

<sup>8</sup>Adiabatically means that the change of the magnetic field during a cyclotron motion is small

```

<!-- CV: POSITION & MOMENTUM -->
<external_define name="pos_r_min" value="0."/> <!-- m -->
<external_define name="pos_r_max" value="0.35e-2"/> <!-- m -->
<external_define name="pos_phi_min" value="0"/> <!-- deg -->
<external_define name="pos_phi_max" value="360"/> <!-- deg -->
<external_define name="pos_z_in" value="12.5"/> <!-- m -->

<external_define name="En_min" value="15.0e3"/> <!-- eV -->
<external_define name="En_max" value="16.0e3"/> <!-- eV -->
<external_define name="mom_th_min" value="0"/> <!-- deg -->
<external_define name="mom_th_max" value="90"/> <!-- deg -->
<external_define name="mom_phi_min" value="0"/> <!-- deg -->
<external_define name="mom_phi_max" value="360"/> <!-- deg -->

```

Figure 19: | **Initialisation of Particle Simulation with Kassiopeia.** The initialization of the particle momentum and position in an xml-file. If a range in energy or position is given particles are generated randomly in the given interval. The initialization xml file defines the simulation.

Kassiopeia uses xml-files as input to describe the experimental set-up and the initialization parameter of the simulation. The structure of an xml-file is shown in figure 19. The particle is initialized with a starting position and momentum. For the binning of the particles it may be advantageous to generate the particles randomly in a certain range. Other parameters of the simulation that are defined in the xml-files are the terminators (conditions that have to be fulfilled to stop the simulation)<sup>9</sup>, the required verbosity of the output as well as the accuracy of the tracking and if adiabatic tracking or exact tracking should be applied.

## 6.1 Electromagnetic Field Computation

Before the particles can be created and tracked first the electromagnetic fields have to be calculated. This is done by `KEMField`. The electromagnetic fields are not given themselves but solely the currents creating them. `KEMField` is an object-oriented toolkit that is designed to solve time-independent electromagnetic problems. As there are no time-dependent electromagnetic fields in the KATRIN set-up, it is sufficient to solve the time-independent Maxwell equations

The Computation is divided into

- **Magnetic Fields**

If the magnetic fields are axisymmetric, the computation can be done via zonal harmonic expansion, which is very fast.

The problem is divided into a *central* and a *remote* part. The remote region thereby ranges from the distance between the source point and the farthest current to infinity [47]. For the

<sup>9</sup>Possible terminators are a minimal or maximal radial or  $z$  component or kinetic energy, a maximal time, a maximal track length or a maximal number of steps

central part the Maxwell equation simplifies to the Laplace equation that is solved by the Legendre polynomials. More details can be found in [48] and [47].

- **Electric Fields**

The electric fields are computed via the **B**oundary **E**lement **M**ethod (BEM): The electrodes are divided into small boundary elements with charge densities described by a system of linear equations. Once the charge density of the elements is known, the potential at any arbitrary point can be calculated by summing the potentials of all boundary elements [45].

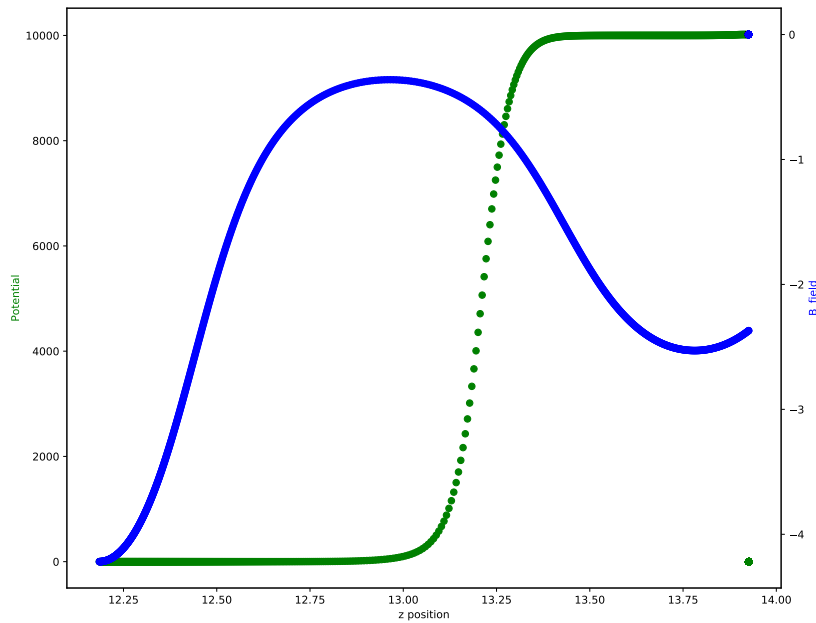


Figure 20: | **Field Configurations.** Result from the electromagnetic field computation for the first tritium settings (see section 8). The figure shows the electromagnetic fields between the main spectrometer and the detector. The magnetic field resulting from the pinch magnet was set to 4.2 T, the field from the detector magnet was 2.5 T. An acceleration voltage of 10 kV was applied between main spectrometer and detector.

## 6.2 Particle Tracking

In KASSIOPEIA there are two possibilities for tracking particles:

- **Exact Tracking**

The motion of a particle with charge  $q$  and velocity  $\mathbf{v}$  that is inside an electric field  $\mathbf{E}$  and a magnetic field  $\mathbf{B}$  is defined by the Lorentz force

$$\mathbf{F} = q (\mathbf{E} + \mathbf{v} \times \mathbf{B}) . \quad (7)$$

If needed the exact trajectory can be calculated. The current state of a particle of mass  $m$  at time  $t$  is defined by its position and momentum vectors  $\mathbf{r}$  and  $\mathbf{p}$ . These quantities can be obtained with the equation of motion (7) and the relativistic momentum  $\mathbf{p} = m\gamma\mathbf{v}$

$$\frac{d\mathbf{r}}{dt} = \frac{\mathbf{p}}{\gamma m} \qquad \frac{d\mathbf{p}}{dt} = q \left( \mathbf{E} + \frac{\mathbf{p} \times \mathbf{B}}{\gamma m} \right) .$$

- **Adiabatic Tracking**

If an-adiabatic effects can be neglected or excluded the adiabatic tracking can be used. This is the case if electric and magnetic fields do not change within a cyclotron rotation.

The movement of the particle consists of a fast circular motion around a point, that is called *guiding center* and a drift that is slow compared to the circular motion. As the Lorentz force acts perpendicularly it does not change the parallel motion on lowest order. Therefore it is possible to split the momentum vector up into a motion parallel  $p_{\parallel}$  and perpendicular  $p_{\perp}$  to the magnetic field. Instead of the position vector, the guiding center of motion  $\mathbf{r}_c$  is calculated. The equations of motion can then be simplified to

$$\begin{aligned} \frac{d\mathbf{r}_c}{dt} &= \frac{p_{\parallel}}{\gamma m} \frac{\mathbf{B}_c}{B_c} \\ \frac{dp_{\parallel}}{dt} &= -\frac{p_{\perp}^2}{2\gamma m B_c} \nabla \mathbf{B}_c + q \mathbf{E}_c \cdot \frac{\mathbf{B}_c}{B_c} \\ \frac{dp_{\perp}}{dt} &= \frac{p_{\parallel} p_{\perp}}{2\gamma m B_c} \nabla \mathbf{B}_c \cdot \frac{\mathbf{B}_c}{B_c} . \end{aligned}$$

The perpendicular motion of the particle depends only on the magnetic field at the guiding center of motion  $\mathbf{B}_c$ , whereas the momentum in parallel direction is changed by the electric field at the guiding center of motion  $\mathbf{E}_c$ .

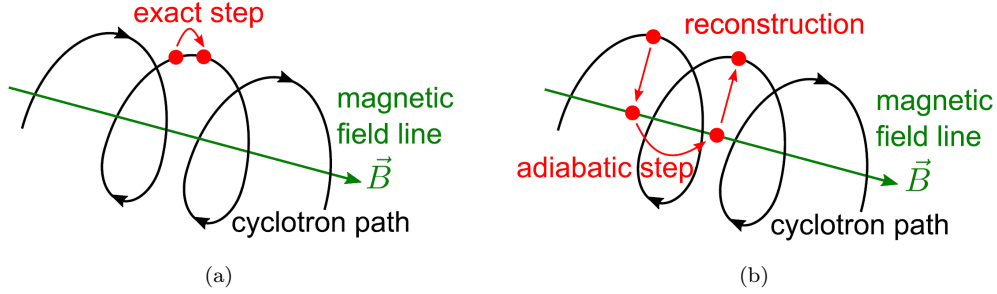


Figure 22: | **Exact and Adiabatic Trajectories.** Visualisation of exact and adiabatic tracking. Picture from [45].

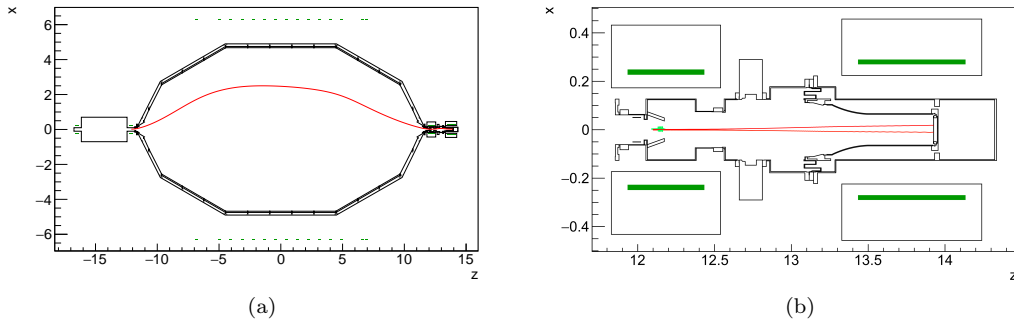


Figure 21: | **KASSIOPEIA Simulations.** Visualisation of output from KASSIOPEIA simulations. Figure (a) shows the movement of one particle in the main spectrometer, in figure (b) the trajectories of two particles can be seen. The particles start behind the main spectrometer and move through the magnetic fields created by the pinch and detector magnet until they reach the detector.

The equations of motions are then solved numerically by the discretisations  $\frac{d\mathbf{p}}{dt} \rightarrow \frac{\Delta\mathbf{p}}{\Delta t}$  and  $\frac{d\mathbf{r}}{dt} \rightarrow \frac{\Delta\mathbf{r}}{\Delta t}$ . All equations are ordinary differential equations of first order and are solved by the Runge-Kutta methods that are provided by KASSIOPEIA.

### 6.3 Particle Interactions

KASSIOPEIA differentiates between space and surface interactions:

- **Space Interaction**

Space interactions occur only with a probability  $P(t)$  and thus are a stochastic process. The probability depends on the time  $t$  the particle is in the medium it interacts with and its

velocity  $v$ :

$$P(t) = 1 - \exp\left(-\frac{tv}{\lambda}\right) \quad (8)$$

where  $\lambda$  is the mean free path of the particle i.e. the path a particle can make before interacting:

$$\lambda = \frac{1}{n\sigma}.$$

This path is shorter for higher target number density  $n$  and a higher cross section  $\sigma$ . The cross section  $\sigma$  is the sum of single cross sections that belong to different types of interactions such as elastic or inelastic scatterings.

Solving equation 8 for  $t$  leads to the time it takes for a scattering to occur

$$t_{scat} = -\ln(1 - P) \cdot \frac{\lambda}{v}$$

where  $P$  is uniformly distributed.

If the step time  $t_{step}$  is shorter than the scattering time  $t_{scat}$ , no scattering will take place. In the cases in which the step time is larger than the scattering time, than the step is shortened so that the step time is equal to the scattering time and the properties of the particle are recalculated and the a scattering will occur. The type of scattering depends on the probabilities and thus the cross sections of the different scattering types.

- **Surface Interaction**

A surface interaction takes place if a particle hits a boundary. The particle can either be transmitted or reflected. Both possible interactions might change the particle's energy and angle.

## 7 Simulation Software: SSC-Sterile

To comply with the requirements of sterile neutrino search, a new software named *SSC-sterile* was developed by Martin Slezák and Alexey Lokhov. It is the counterpart to the SSC software within KASPER (used for mass measurement) for sterile neutrino search. In this chapter I explain why a new simulation software is required and the model building approach used by SSC-sterile.

### 7.1 Requirement of New Simulation Software for Sterile Neutrino Search

The software currently used for modelling the  $\beta$ -decay spectrum is highly specialised for the neutrino mass measurements which stay in a region of a few tens of eV from the endpoint.

However when looking deeper into the spectrum, effects<sup>10</sup> negligible in the endpoint region will become important. This includes

- **Rear Wall**

Electrons that get scattered back from the rear wall lose energy during the scattering. For the mass measurement these electrons do not have an impact on the spectrum: the retarding potential is too high preventing the electrons from passing through the spectrometer. On the other hand these electrons indeed are important for sterile neutrino search. Measuring far below the endpoint, the retarding voltage is low enough to let the electrons pass the spectrometer and reach the detector. The backscattering at the rear wall has been simulated with GEANT4.

- **Source**

In the WGTS the electrons scatter with gas molecules. The energy loss for scattering once is shown in figure 15. However the energy loss function is modelled under the assumption that electrons have energies near the endpoint region making it energy independent. At lower retarding potentials this assumption is no longer valid: The scattering cross-section gets energy dependent. This influences the energy loss due to scatterings but also the scattering probability.

Moreover multiple scatterings ( $> 10$  times) have to be considered, because electrons that start with high energies may still be in the region of interest although they lost energy in scattering processes. The calculation of the source scattering is done with a convolution code that has been developed by Martin Slezák.

- **Detector**

Electrons that reach the detector will not necessarily deposit all of their energy in the sensitive part of detector. The detector has a so called *dead-layer*. If the electron scatters in the dead-layer this energy deposition will not be seen. This effect is energy dependent as the scattering cross-sections are energy-dependent, too.

This is even more crucial for the second phase of data taking because the measured spectrum will be differential: For the first phase of data taking the quantity taken into account is the count rate depending on the retarding potential whereas for the differential measurement the energy distribution is of prime importance.

---

<sup>10</sup>Effects that are new are in sterile neutrino search are all connected with scattering of electrons. However, there are effects like magnetic reflection that do not change the electron's energy and therefore do not have an direct influence on the spectrum but they could still be important when they are combined with other effect.

Moreover, electrons can be backreflected in either the retarding potential, the pinch magnet or the post acceleration voltage, that is applied between MS and Detector, after being scattered back from the detector.

Another effect that could be crucial is the dependence of the detection efficiency<sup>11</sup> on the retarding potential: The backscattered electrons could pass the retarding potential and reach the source again. This is more likely to happen for low retarding potentials and therefore has no effect for the mass measurement using only high retarding potential. However in case of sterile neutrino search [49] this effect does play a role. The detector has been simulated with KASSIOPEIA (this thesis) and KESS.

---

<sup>11</sup>The detection efficiency is a quantity that describes how the measurement result deviates from the result that would be measured by a perfect detector.

## 7.2 Modelling the Tritium Beta Decay Spectrum with SSC-sterile

SSC-sterile is designed to model the tritium  $\beta$ -decay spectrum that will be measured in the detector for sterile neutrino search.

The main idea of building the model in SSC-sterile is to

1. divide the KATRIN set-up into several components namely the Rear Wall, the Source, the Main Spectrometer and the Detector and calculate how this parts correspond to monoenergetic<sup>12</sup> and monoangular electrons.
2. combine the responses of the single components to an overall response.

SSC-sterile represents the two dimensional energy-angle spectrum as an array where each entry refers to the percentage of electrons with the angle and energy aligned to this array position. This means that an initial monoenergetic and monoangular spectrum is represented by a vector with only values 0 except for one entry that is 1. This array (representing a spectrum) gets transformed by a matrix (representing the response of one component) as shown in figure 26. For each initial angle and energy a separate response matrix is needed as the transformation depends on this properties. So all in all for a spectrum that is divided into  $n$  energy and  $m$  angular bins  $n \cdot m$  two-dimensional response matrices are needed to characterize one component completely<sup>13</sup>. Combining these two-dimensional matrices leads to a four-dimensional matrix for each component. The four-dimensional matrices of the components are the input that SSC-sterile needs for building an overall response and calculate the model for the sterile neutrino spectrum. This matrices do not necessarily have to be unitary. Electrons may get lost or absorbed by the component and thus the norm of the array does not have to be conserved.

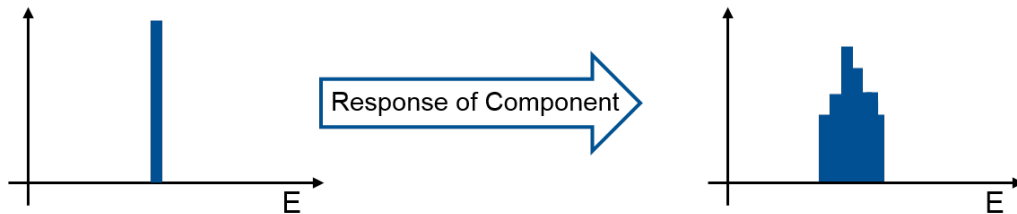


Figure 23: | **Transformation of Monoenergetic Particles.** Visualisation of how the component transforms the initial monoenergetic spectrum. For simplicity the illustration is reduced to one dimension.

If the responses are known for all angles and energies, the transformation of an *arbitrary* energy spectrum can be calculated as every spectrum can be approximated as a superposition of the monoenergetic bins. So for the transformation of a whole energy spectrum the single responses have to be weighted with the amplitudes of the mono-energetic bins in the initial spectrum.

<sup>12</sup>Although I am referring to the electrons as monoenergetic and monoangular strictly speaking they are not, but consist of a uniformly and randomly distributed starting angles and energies in the particular interval.

<sup>13</sup>A specific case is the detector response that has only information about the outgoing (detected) energies and therefore has just an one-dimensional output. The information on the angle is not needed as the detector is the last component the particles have to pass and moreover the distribution in angle is not measured.

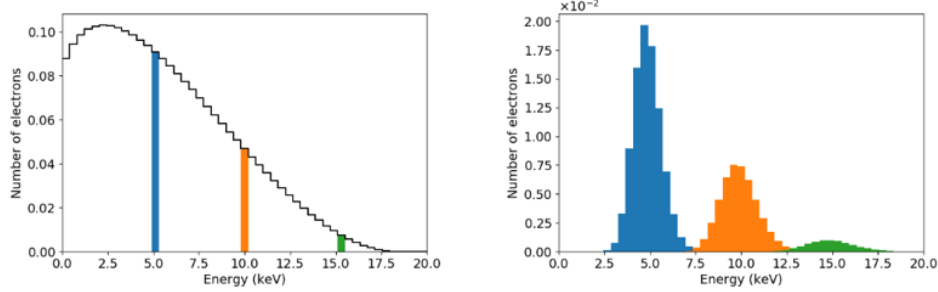


Figure 24: | **Transformation of Spectrum.** Any arbitrary energy spectrum can be considered as a linear superposition of monoenergetic bins. As the response of the component to the monoenergetic electrons is known, so is the response to the whole spectrum. Figure from [50].

After completing the first step which is computing the response of the single components, they can be combined to an overall response of the whole experimental set-up. This combination is done by convolving the responses. If the initial spectrum is given by  $\mathbf{S}_{\text{ini}}$  and transformed by the components  $R_i$  to the final spectrum  $\mathbf{S}_{\text{fin}}$  this yields

$$\mathbf{S}_{\text{fin}} = R_1 \times R_2 \times R_3 \times \dots \mathbf{S}_{\text{ini}}$$

The most simple possibility of how an electron can make it to the detector would be reaching the detector directly after being created in the source and passing the main spectrometer. In this case, the responses of the source  $R_S$  and the detector  $R_D$  are needed. The response of the main spectrometer can be calculated easily as it is mainly defined by the particle's energy. It will either pass the main spectrometer or be rejected, hence, is either 1 or 0. The most simple spectrum  $\mathbf{S}_{\text{simple}}$  considering only electrons reaching directly the detector without any backscattering is then given by

$$\mathbf{S}_{\text{simple}} = R_D \times R_S \times \mathbf{S}_{\text{ini}}$$

However there are numerous possibilities to be taken into account: it may be the case that the electron starts moving towards the rear wall, gets backscattered there and passes the main spectrometer directly or even after multiple backscatterings between the rear wall and source [51]. Backscattering that occurs in the detector section is modelled and taken into account in the detector response as well as the reflection by magnetic mirrors at the pinch magnet for electrons with large angles. To obtain the final spectrum all the tracks that have a non-negligible effect, have to be summed up.

$\cos(\theta_{ini}) \backslash E_{ini}$	$E_1$	$E_2$	$E_3$	...
$\cos(\theta_1)$	$\begin{pmatrix} R_{1111} & R_{1112} & R_{1113} \\ R_{1121} & R_{1122} & R_{1123} \\ R_{1131} & R_{1132} & R_{1133} \end{pmatrix}$	$\begin{pmatrix} R_{2111} & R_{2112} & R_{2113} \\ R_{2121} & R_{2122} & R_{2123} \\ R_{2131} & R_{2132} & R_{2133} \end{pmatrix}$	$\begin{pmatrix} R_{3111} & R_{3112} & R_{3113} \\ R_{3121} & R_{3122} & R_{3123} \\ R_{3131} & R_{3132} & R_{3133} \end{pmatrix}$	
$\cos(\theta_2)$	$\begin{pmatrix} R_{1211} & R_{1212} & R_{1213} \\ R_{1221} & R_{1222} & R_{1223} \\ R_{1231} & R_{1232} & R_{1233} \end{pmatrix}$	$\begin{pmatrix} R_{2211} & R_{2212} & R_{2213} \\ R_{2221} & R_{2222} & R_{2223} \\ R_{2231} & R_{2232} & R_{2233} \end{pmatrix}$	$\begin{pmatrix} R_{3211} & R_{3212} & R_{3213} \\ R_{3221} & R_{3222} & R_{3223} \\ R_{3231} & R_{3232} & R_{3233} \end{pmatrix}$	
$\cos(\theta_3)$	$\begin{pmatrix} R_{1311} & R_{1312} & R_{1313} \\ R_{1321} & R_{1322} & R_{1323} \\ R_{1331} & R_{1332} & R_{1333} \end{pmatrix}$	$\begin{pmatrix} R_{2311} & R_{2312} & R_{2313} \\ R_{2321} & R_{2322} & R_{2323} \\ R_{2331} & R_{2332} & R_{2333} \end{pmatrix}$	$\begin{pmatrix} R_{3311} & R_{3312} & R_{3313} \\ R_{3321} & R_{3322} & R_{3323} \\ R_{3331} & R_{3332} & R_{3333} \end{pmatrix}$	
...				

Figure 25: | **Response Matrix.** Visualisation of response matrix that characterises one component for the case of three bins per dimension. Each initial bin is monoenergetic and monoangular and results in an output matrix. The output matrix describes how the component transforms electrons with the specific initial energy and angle. The matrix element  $R_{ijkl}$  describes how many percent of the electrons that arrive at the component and have an initial energy  $E_i$  and initial angle  $\cos(\theta_j)$  will have a final energy  $E_k$  and final angle  $\cos(\theta_l)$  after passing the component. For a binning of  $n \times m$  in energy and angle this leads to  $n \cdot m$  two dimensional matrices that are needed to characterise a component completely.

### 7.3 Modelling of the Detector Response

One of the four main components that has to be characterised regarding how it acts on an energy spectrum, is the detector part of the KATRIN experiment. The KATRIN detector is a silicon detector consisting of 148 pixel elements with an energy resolution of 3 keV.

The two effects that transform the incoming energy spectrum are the finite energy resolution and the dead layer. The finite energy resolution smears the energy spectrum and is mathematically a convolution with a Gaussian function. The dead layer denotes the part of the detector which cannot measure energy. If energy is deposited in this part of the detector it will not be measured and thus will not appear in the energy spectrum. The simulation takes into account the dead layer and backscattering effects on the spectrum, the smearing due to the finite energy resolution and an energy cut-off at 5 keV are applied afterwards to the simulated spectrum.

#### 7.3.1 Simulation Settings

The detector response is simulated with the KASSIOPEIA simulations software. The simulation parameters for the detector response were chosen to be

- **initial position**

The flux tube  $\Phi$  is given by

$$\Phi = \int_C \mathbf{B} \, d\mathbf{S}$$

where the magnetic field  $\mathbf{B}$  and the surface element  $d\mathbf{S}$  are integrated over the surface limited by the closed curve  $C$ . Due to Gauß law for magnetic fields ( $\nabla \cdot \mathbf{B} = 0$ ) this quantity has to be constant. It follows that the strength of the flux tube increases if it widens, and decreases if it narrows [52]. If the magnetic field  $B$  is homogeneous in the enclosed surface the equation can be simplified to

$$\Phi = A \cdot B = \pi r_{max}^2 B$$

where  $A$  is the enclosed surface by the radius  $r_{max}$ . The magnetic field in the starting point  $B_S = 4.2$  T and the magnetic field in the detector magnet  $B_{det} = 2.52$  T are given. The radius of the detector is  $r_{det} = 4.5$  cm. Due to the constant magnetic flux tube, the maximal radius  $r_{max}$  of the particles at the starting point able to reach the detector position within the detector radius, is given by

$$r_{max} = \sqrt{\frac{\Phi}{\pi B_S}} = \sqrt{\frac{\pi r_{det}^2 B_{det}}{\pi B_S}} = r_{det} \sqrt{\frac{B_{det}}{B_S}}$$

The radius of the disk that defined the starting positions of the electrons was chosen to  $r_{max}$ . The starting position  $z_S$  (where the  $z$ -axis is given by the beam line) was the position of the maximal magnetic field

$$z_S = 12.18 \text{ m}.$$

The origin of the coordinate system thereby lies in the middle of the main spectrometer.

- **initial energy**

The endpoint of the tritium  $\beta$ -decay is near  $E_0 = 18.575$  keV. Therefore electrons between  $E_{min} = 16.575$  keV and  $E_{max} = 18.575$  keV were simulated distributed into five energy bins to get the response to all energies that an electron from the  $\beta$ -decay can have when a retarding voltage of 16.575 kV applied to the main spectrometer. Each simulation consisted of 10000 simulated  $\beta$ -decay electrons.

The final output binning is chosen later after finishing the simulation and does not depend on the input binning. The detector is the last response acting on the spectrum. Electrons that are able to escape through the main spectrometer will scatter in the source and the rear wall and hence not come back to the detector.

- **initial angle**

For the simulation the electrons were set to start in the pinch magnet. Therefore the electrons move towards a lower magnetic field which does not evoke magnetic reflection. Only in the case of back scattering, the particles move towards the higher magnetic field. Particles with large angles get reflected by the higher magnetic field.

The particles were generated monoangularly between  $\cos\theta_{min} = 1$  and  $\cos\theta_{max} = 0$  and in five bins as well. The distribution in  $\phi$  direction was chosen to be isotropic.

### 7.3.2 Results

The results of the simulation can be seen in the following. Figure 26 shows the effect the detector has on the spectrum: In a) the raw simulation data is displayed. The initial energies are in an interval that ranges from 17.375 to 17.775 keV. The peak in the spectrum is shifted 10 keV to the right because of the 10 kV acceleration voltage acting on the electrons between main spectrometer and detector. The energy distribution of the raw data is mainly defined by the dead layer of the detector, that was set to 100 nm.

The histogram in b) shows the detector response taking into account dead layer effects and the finite energy resolution as well as the energy cut-off at 5 keV. The energy resolution of the KATRIN detector system is rather high which leads to a smearing of the spectrum. Energies below 5 keV are not detected.

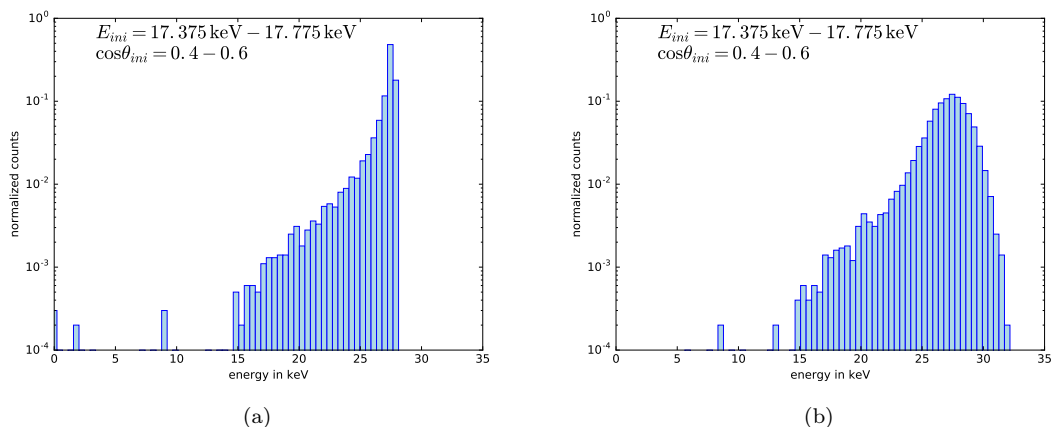


Figure 26: | **Response Matrices.** Visualisation of response matrices with and without smearing. a) The histogram displays the raw energy transformation due to the detector section, b) the histogram also takes into account the finite energy resolution of 3 keV of the detector.

Figure 27 shows the energy spectra when a) considering only the energy deposition in the detector of the first hit and b) the total energy deposition resulting from all hits. In case of backscattering electrons can hit the detector for another time. If they reach the detector for a second time they have either been reflected in the main spectrometer ( $E < U_{MS}$ ) or from the post acceleration voltage ( $E_{||} < 10$  keV) because their total energy is too low or their angles are too large. If an electron hits the detector and deposits energy in the sensitive part of the detector for another time, the energies are summed up. This explains the spectrum displayed in the histogram in b) that contains more entries in the high energy region and less entries in the lower energy region: the entries were shifted towards the higher energy region due to the addition of all energy depositions.

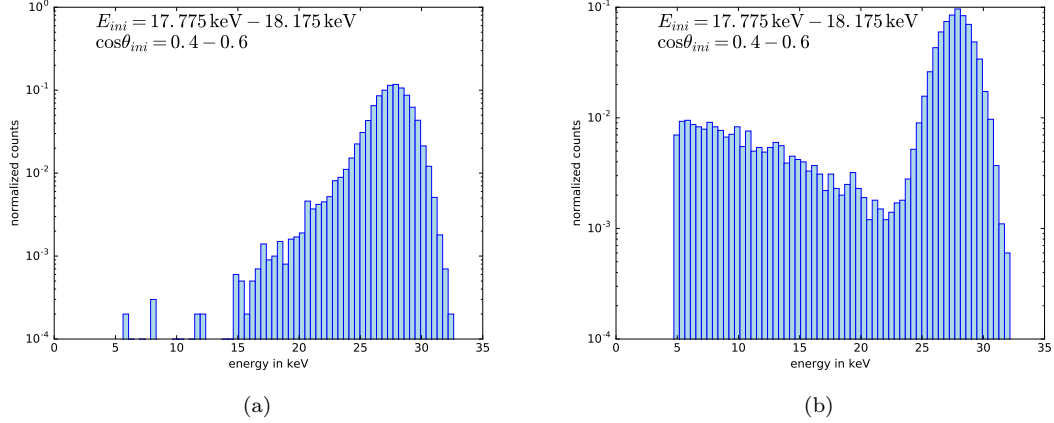


Figure 27: | **Backscattering in Detector.** The figure shows the energy spectrum resulting from a) considering only the energy deposition when hitting the detector for the first time and b) considering the total energy deposition of all hits.

## 7.4 Retarding Potential Dependence

As described in section 7.1 an effect that is not considered for neutrino mass measurement is the dependence of the detector efficiency on the retarding potential. Electrons that scatter back from the detector may still be high energetic enough to overcome the retarding potential. The probability of this to happen increases with decreasing retarding potential.

### 7.4.1 Simulation Settings

To investigate how the retarding potential impacts the energy spectrum, monoenergetic electrons were simulated in set-ups with varying retarding potential.

The electrons started with energies of 10 keV and uniformly distributed angles in the pinch magnet before being accelerated by an acceleration voltage of 10kV.

In contrast to the simulation settings for the detector response matrices, the retarding potential was varied ( $U_{MS} = 0\text{ kV}, 5\text{ kV}, 10\text{ kV}$ ) whereas initial energy and angle ranges were the same for all simulations. The statistic was increased to 700000 particles for each retarding potential.

### 7.4.2 Results

The histogram in figure 31 displays only the energy of the first energy deposition of the electrons that are left with enough energy to make it to the main spectrometer overcoming the acceleration voltage. The energy spectra are very similar because the first energy deposition is independent from the retarding potential. In contrast, the histograms displaying all energies deposited in the sensitive part of the detector are displayed in figure 32. The histogram in a) shows the raw data, b) the smeared data. The difference in the spectra of the varied retarding voltages appears in the energy

	16.575 keV	16.975 keV	17.375 keV	17.775 keV	18.175 keV
0.0 keV	0.0	0.0	0.0	0.0	0.0
1.8 keV	0.0	0.0	0.0	0.0	0.0
3.6 keV	0.0	0.0001	0.0	0.0	0.0
5.4 keV	0.0002	0.0001	0.0001	0.0	0.0001
7.2 keV	0.0	0.0002	0.0003	0.0001	0.0001
9.0 keV	0.0001	0.0	0.0	0.0002	0.0002
10.8 keV	0.0003	0.0005	0.0002	0.0002	0.0001
12.6 keV	0.0007	0.0006	0.0004	0.0002	0.0004
14.4 keV	0.001	0.0007	0.0008	0.0009	0.0005
16.2 keV	0.0022	0.002	0.0019	0.0016	0.0016
18.0 keV	0.0061	0.0043	0.005	0.0041	0.0031
19.8 keV	0.0128	0.0099	0.008	0.0064	0.0072
21.6 keV	0.0247	0.0205	0.0175	0.0169	0.0133
23.4 keV	0.0938	0.0755	0.0549	0.0395	0.0311
25.2 keV	0.3545	0.3008	0.2521	0.207	0.1594
27.0 keV	0.4041	0.4436	0.4618	0.4563	0.4411
28.8 keV	0.0956	0.1346	0.1835	0.2426	0.3027
30.6 keV	0.0034	0.0063	0.0132	0.0235	0.0381
32.4 keV	0.0	0.0	0.0	0.0003	0.0008
34.2 keV	0.0	0.0	0.0	0.0	0.0
36.0 keV	0.0	0.0	0.0	0.0	0.0
37.8 keV	0.0	0.0	0.0	0.0	0.0
39.6 keV	0.0	0.0	0.0	0.0	0.0
41.4 keV	0.0	0.0	0.0	0.0	0.0
43.2 keV	0.0	0.0	0.0	0.0	0.0

Figure 28: | **Detector Responses.** The table shows the probabilities for an energy deposition between 0 and 45 keV (rows) when the electron has an initial energy between 16.575 and 18.575 keV (column) for  $\cos\theta = [0.8, 1]$ . The energies are the minimal energies of the bins.

region below 10 keV. To explain this effect one can think about what happens to an electron that leaves  $x$  keV in the detector:

A electron that leaves  $x$  keV in the detector stays with  $(20 - x)$  keV before and  $10 - x$  keV after passing the acceleration voltage in backward direction. Depending on the retarding voltage the electron could now overcome the potential barrier which is the case if  $U_{ms} < (10 - x)$  kV and therefore is lost and cannot change the energy bin resulting from the first hit. In contrast, the electrons get backscattered towards the detector if the retarding potential is high enough ( $U_{ms} > (10 - x)$  kV). This means that they can hit the detector for a second time and the energy they leave in the detector this time gets added to the already existing energy bin from the first hit. Hence the energy bins disappear from their original position and are shifted towards higher energies. For a high retarding potential none of the backscattered electrons can pass the main spectrometer and therefore they hit the detector for a second time and the energy bins are shifted. For a low retarding potential electrons may not be back-reflected and may not reach the detector for a second time. These energy bins do not change. For intermediate potential only the electrons that left enough energy in the detector to not be able to escape through the main spectrometer return, whereas electrons that only left small amounts of energy do still carry enough energy to pass the main spectrometer and cannot return to change the spectrum. This explains the sharp decrease in the spectrum that was simulated with retarding voltage of 5 kV in the main spectrometer.

Including the smearing and energy cut-off the spectra get transformed to figure 32 b). The dependence on the retarding potential of the detection efficiency has to be included when building the  $\beta$ -decay model.

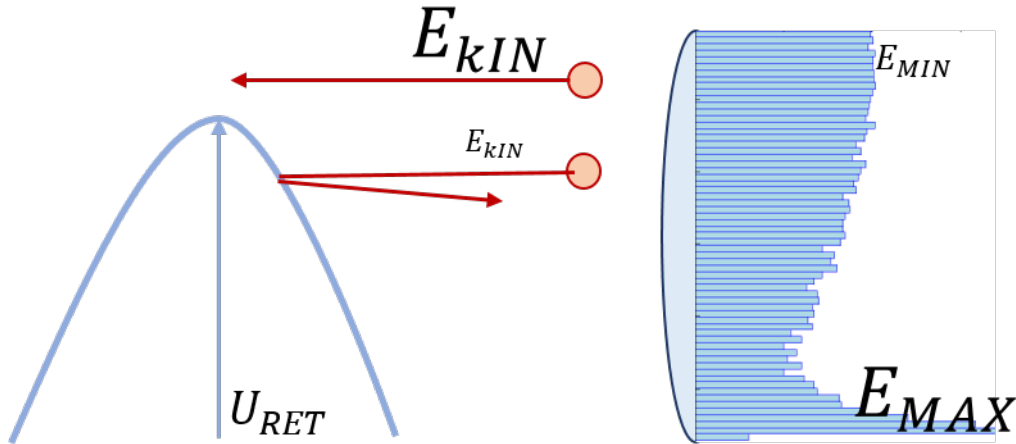


Figure 29: | **Retarding Potential Dependence.** An electron that leaves a high amount of energy in the detector will be too low-energetic to overcome the retarding potential in the main spectrometer. But if an electron deposits only a small amount of energy in the detector it may still be high energetic enough to pass the main spectrometer and cannot hit the detector a second time.

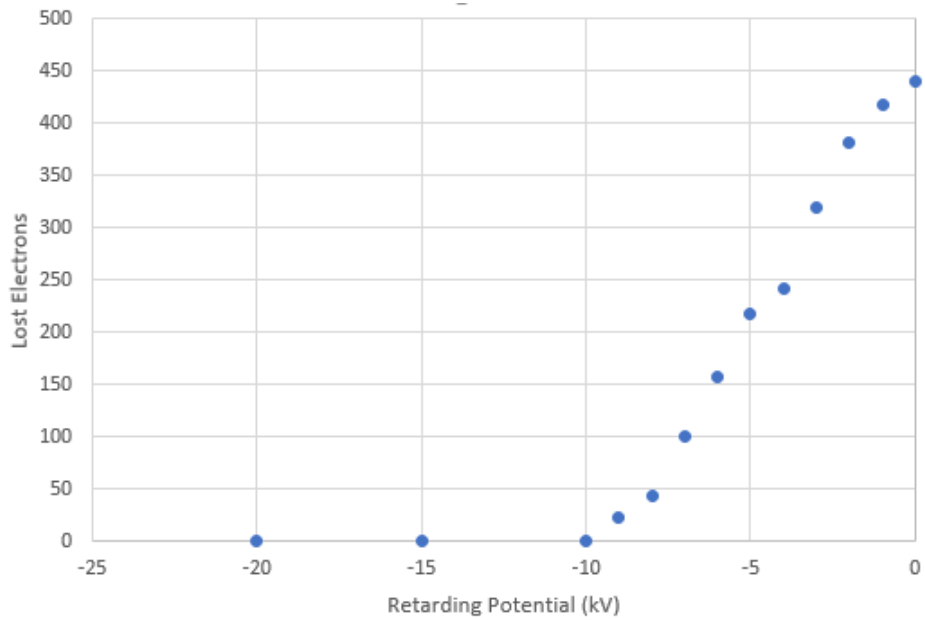


Figure 30: | **Detection Efficiency.** The Graph shows the number of electrons that overcome the retarding potential in the main spectrometer and can therefore not hit the detector for a second time. 100000 electrons were started with energies of 10 keV and an isotropic angular distribution. Retarding potentials that are higher than 10 kV let not pass any electrons. The lower the retarding potential, the more electrons can pass. This dependence of the detection efficiency on the retarding potential has to be considered when building the tritium  $\beta$ -decay model.

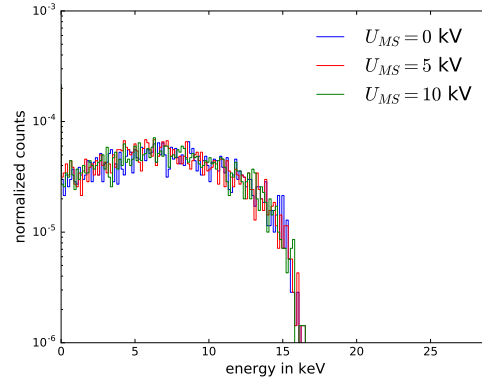


Figure 31: | **Backscattering Spectra.** The histogram shows the first energy deposition in the sensitive detector part of electrons that are backscattered, overcome the acceleration voltage and pinch magnet and reach the main spectrometer. Up to this point there is no difference besides statistical fluctuations as only the first hit is considered and the electrons have not yet seen the retarding potential.

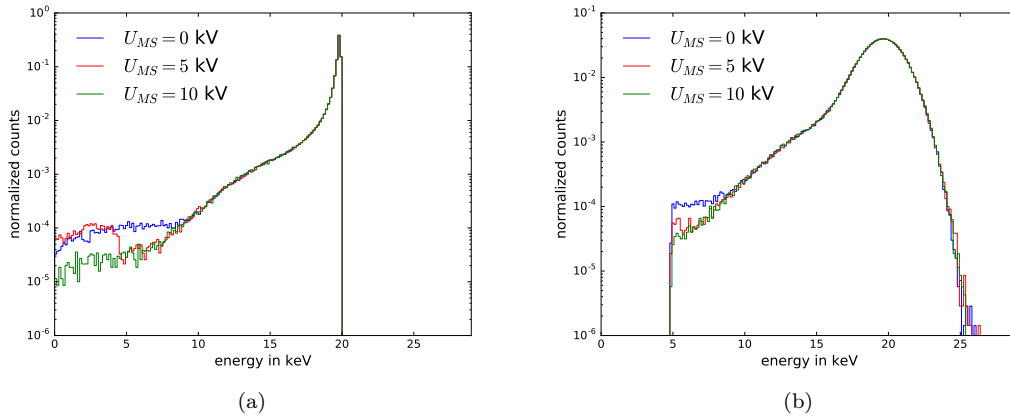


Figure 32: | **Final Energy Deposition.** The histogram contains all energy of all hits that was deposited in the sensitive part of the detector. The effect of the retarding potential in the main spectrometer becomes apparent in the region below 10 keV. The figure in a) shows the spectra without including the final energy resolution and the cut-off. The histogram in b) shows how the effect would look like in the real measurement where the detector smears the energy distribution.

## 8 Analysis of First Tritium Data for Sterile Neutrino Search

The data taken during the First Tritium Campaign can be used to make a first analysis with respect to sterile neutrino search. In this chapter first an introduction to the measurement campaign will be given, then the analysis strategy and its results will be presented.

### 8.1 First Tritium Campaign

The “First Tritium Campaign” refers to the first phase<sup>14</sup> of data taking where tritium was injected into the WGTS and the first scans were performed.

The FT Campaign took place from 5<sup>th</sup>-18<sup>th</sup> June 2018 and consisted of 24 1-hour runs, 64 1.5-hour runs and 31 3-hour runs. Although not all of the runs are dedicated sterile scans they can be used for sterile analysis and give new results for sterile neutrino search. For this thesis the data from 3-hour runs was used. The scans went down up to 1.6 keV below the endpoint. This means that the analysis will be most sensitive to a neutrino mass below 1.6 keV. The measurement time distribution of the scans used in this thesis is shown in figure 33.

### 8.2 Configuration for First Tritium Measurements

The measurements were taken according to the **M**asurement **T**ime **D**istribution (MTD) as seen in figure 33. The setting of magnetic fields as well as the source properties can be found in the table 2.

Table 2: | **Configuration for First Tritium.** The table shows the configurations that were used for the analysis model that were chosen according to the settings from the first tritium measurement campaign.

<b>KATRIN Configuration</b>	
Quantity	Value
Magnetic Field Analyzing Plane	6 G
Magnetic Field Pinch	4.2 T
Magnetic Field Source	2.52 T
Column Density	$\sim 4.5 \times 10^{17} \frac{\text{molecule}}{\text{cm}^2}$
TT concentration	$\sim 0$
DT concentration	$\sim 1$
HT concentration	$\sim 0$

<sup>14</sup>Strictly speaking the first phase of data taking were four scans in the “Very First Tritium Campaign”. But **F**irst **T**ritium (**FT**) provides much higher statistics and the results in this thesis are based only on the measurements from **FT**.

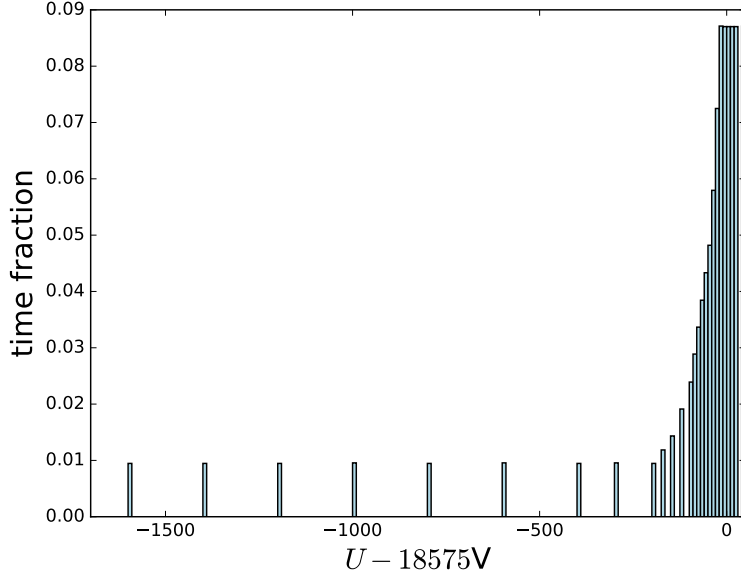


Figure 33: | **Measurement Time Distribution (MTD)**. The data used in this thesis was taken according to this measurement time distribution. The time fractions are given relative to the total measuring time of three hours. Near the endpoint of the  $\beta$ -decay spectrum the count rates get lower. To compensate for this effect the measurement time and density of data points is increased towards the endpoint region.

### 8.3 Physics Model

The fits were performed with `Fitrium` which was developed in the KATRIN group in Munich in the Max Planck Institute for Physics by Martin Slezák and Christian Karl [17]. The model used in `Fitrium` is the theoretical tritium  $\beta$ -decay spectrum, that is transformed by the response function that is defined by the setting in the WGTS and the main spectrometer. Afterwards pixel- and energy-dependent detection efficiency is applied to the model in order to correct for the effects described in section 8.3.2.

#### 8.3.1 Spectrum and Response

The tritium spectrum for sterile neutrinos comes with two additional parameters: the mixing angle  $\theta_S$  that only appears as  $\sin^2 \theta_S$  in the analysis and the mass of the additional mass eigenstate  $m_4$ . The effective mass of the light neutrinos  $m_\beta$  was set to 0. This modifies the spectrum  $\frac{d\Gamma}{dE}(m_\beta)$  from equation 5 to

$$\frac{d\Gamma}{dE}(\theta_S, m_4) = \cos^2 \theta_S \cdot \frac{d\Gamma}{dE}(m_\beta = 0) + \sin^2 \theta_S \cdot \frac{d\Gamma}{dE}(m_4).$$

This spectrum is transformed by the KATRIN set-up due to scatterings in the source and the cut-off in the main spectrometer. The KATRIN response function is explained in more detail in

section 4.4. The model considers up to 10 scatterings in the source, the magnetic field settings are according to the configuration in table 2.

Another point that has to be taken into account FSD: The distribution of the final states can be calculated theoretically and is included in the fit model according to [53].

### 8.3.2 Detection Efficiency

There are several effects that have an influence on the detection efficiency and thus are included in the model to improve the goodness of fit. The effects described below have been presented in [54]. The detection efficiency is especially for sterile neutrino search of importance: The detection efficiency depends on the retarding potential (see section 7.4). This could change the count rates measured at each retarding potential relative to each other.

#### ROI-Cut Loss

For high retarding potentials close to the endpoint the incoming electrons are nearly monoenergetic in contrast to electrons passing smaller retarding potential and the incoming spectra have different shapes. A **Region Of Interest (ROI) Cut** is performed to exclude background. But the cut does not only exclude background but also  $\beta$ -decay electrons. The amount of excluded events depends on the shape of the spectra and on the retarding potential and leads to an decreasing detection efficiency for smaller retarding potentials.

#### Non-Uniformity

One effect that influences the detection efficiency is the pixel non-uniformity that is illustrated in figure 34. The figure shows the relative efficiency of all pixels of the detector. This efficiency depends on the region of interest (ROI) that is taken into account. For a smaller region of interest the measured rates differ from pixel to pixel whereas for a larger region the rates differ less. This is due to non-uniformity of the different pixels. The energy resolution is not the same and thus some pixels smear the energy of the incoming electrons more than others. For pixels with a higher energy resolution and thus less smearing more electrons are detected as for pixels with a lower energy resolution.

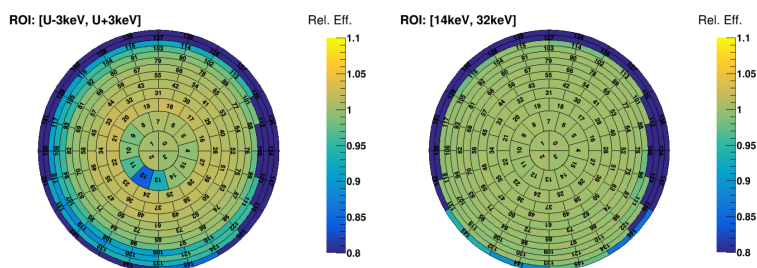


Figure 34: | **Pixel Non-Uniformity.** The pixel rates were taken from a stability run. The difference between the pixel rates are caused by the region of interest cut. This denotes that pixels have different energy resolutions. Picture from [54].

#### Backscattering Loss

The backscattering loss has already been explained in section 7.4.2: An electron that is scattered back in the detector may have enough energy to overcome the retarding potential in the main spectrometer. An electron that passes the main spectrometer in the direction to the source will not hit the detector again and therefore the energy left is not detected.

The lower the energy that is deposited in the detector the higher the probability that backscattering

loss occurs. This leads to an retarding potential dependent detection efficiency that has to be included into the model.

### Pile-Up Loss

It may be the case that an electron is detected and within a certain time interval a second electron hits the detector. Its energy is summed up to the first event and thus two electrons are counted as one event. This effect is called “pile-up”. The events originating from the pile-up lead to detected energies above the endpoint and missing energies in the spectra. The pile-up effect increases for smaller energies and this energy dependence of the detection efficiency has to be taken into account and corrected. The effect can be seen in figure 35: The energies of more than one electron are summed up and lead to detected energies above the actual endpoint.

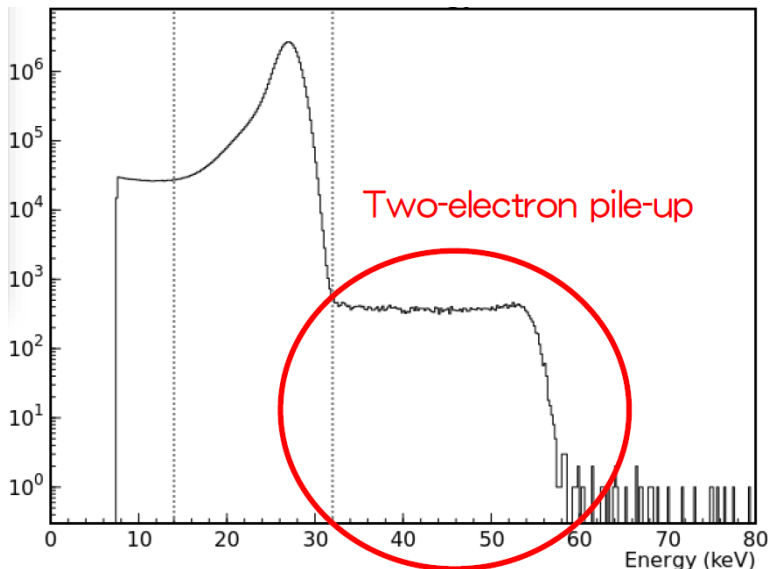


Figure 35: | **Pile-Up loss.** If two particles are registered in the detector within a certain time interval they are not resolved as two events but their deposited energies are summed up. This leads to an falsely detected energies even above the endpoint. This effect is known as pile-up. Picture from [54].

## 8.4 Analysis Strategy

To exclude sterile mass and angle pair  $(m_4, \sin^2 \theta_s)$  a two dimensional scan through the parameter space spanned by angle and mass was performed. This means that for each fit the sterile mass and the sterile mixing angle is fixed to different values. The only parameters left free for the fit are the background, the normalization and the endpoint. The latter will become important later when investigating the fit stability.

If there is a large disagreement between model and measured data, the parameters used in the model can be excluded. If the fit result at each grid point is known, it can be used to interpolate to the fit results of the intermediate points. Regions in parameter space that have a bad fit result can be excluded in this way.

### 8.4.1 Selection and Combination of Pixels and Runs

For the analysis presented in this work a single run (40667) was chosen. The full energy range down to 1.6 keV below the endpoint was used. Finally, since the Forward Beam Monitor [55] shadowed some of the detector pixels, 28 pixels (100, 112 and 123 - 148) were excluded from the analysis. For the fit the so-called “uniform-fit” was used: the counts of all pixels at the respective retarding potential were summed up. This corresponds to treating the detector as one large pixel. Here, before summing up the count rates of the single pixels, they are corrected for the detection efficiency for each pixel individually.

## 8.5 Statistical Method

The aim of fitting a data set to a model is to align the parameters to achieve the best possible agreement. The fit is done with the maximum likelihood estimation. If a model includes the parameters  $\theta$  and the data that has been measured is  $\mathbf{x}$ , the likelihood of the fit is given by

$$\mathcal{L}(\mathbf{x}|\theta) = \prod_i f(x_i|\theta)$$

where  $f$  is the probability distribution. To get the parameters that fit best to the model, the parameters with the maximum likelihood have to be found. This is equal to minimizing the negative logarithm of the likelihood

$$-\ln \mathcal{L}(\mathbf{x}|\theta) = -\sum_i \ln f(x_i|\theta).$$

In **Fitrium** a Poisson, a Gaussian and a Gaussian with **Covariance Matrix** (CM) function are available. For a Gaussian function the maximum likelihood fit reduces to the usual  $\chi^2$ -fit. If the fit is performed with varied sterile mixing angle and neutrino mass (scanning the  $\theta_s$ - $m_4$  space), this leads to a different negative  $-\ln \mathcal{L}(\mathbf{x}|\theta)$  for each parameter pair and a highest likelihood for one parameter pair. If a fit deviated too much from the best fit it is so unlikely to be true that it can be excluded: A point in the parameter space can be excluded with 90% C.L., if:

$$\Delta(-\ln(\mathcal{L})) \equiv (-\ln(\mathcal{L})) - (-\ln(\mathcal{L}_{min})) \geq 2.3$$

## 8.6 Treatment of Systematics

The systematics that are taken into account for the data analysis are

- **Maximal Magnetic Field**

The maximal magnetic field in the pinch magnet is included in the KATRIN response function (see section 4.4). A higher maximal magnetic fields would reduce the transmission probability of the electrons that goes into the model due to magnetic reflection. Its uncertainty was assumed to be 2%.

- **Magnetic Field Analysing Plane and Magnetic Field Source**

The energy resolution of the MAC-E filter depends on ratio of the magnetic field in the analysing plane and the magnetic field in the source: the smaller the ration  $\frac{B_A}{B_S}$ , the higher the energy resolution of the MAC-E filter. They are included in the transmission function of the KATRIN response function. Both of these magnetic field uncertainties were set to 2%.

- **FSD onset**

The onset on the FSD is a deviance from the probabilities for the tritium to be in the ground or excited states, that are given in [53]. The uncertainty used in this thesis is 0.03.

- **Column Density**

The uncertainty on the column density describes the absolute uncertainty on all scans. An increased column density will lead to an increased rate and an increased scattering probability of the electrons. This would change the normalization of the spectrum as well as the actual shape due to scatterings. A precise knowledge of the column density is crucial for succeeding in the measurement and its uncertainty has to be taken into account for data analysis. The value for the uncertainty of the column density used in this thesis is 5%.

- **DT Fluctuation**

In contrast to the column density, the DT fluctuation refers to the variation of the amount of tritium during a scan. If the tritium amount varies this could lead to varying count rates during the scan. This could manifest in a kink in the  $\beta$ -decay spectrum and hence imitating a sterile neutrino. To exclude this non-physical sterile neutrino the uncertainty on this quantity is considered when fitting the sterile neutrino spectra. In contrast to the column density this effect is uncorrelated (CM with only diagonal elements) as the time scale of the fluctuations is too small to lead to a correlation between neighboured data points. The uncertainty value of the DT fluctuation was set to  $10^{-3}$  for this analysis.

### 8.6.1 Including Systematics with the Covariance Matrix

All systematics are included with the **Covariance Matrix (CM)** approach: If  $\mathbf{X}$  is a vector of randomly distributed variables with a finite variance, its CM  $\Sigma$  is defined as

$$\Sigma = \begin{pmatrix} Var[X_1] & Cov[X_1, X_2] & \cdots & Cov[X_1, X_n] \\ Cov[X_2, X_1] & Var[X_2] & \cdots & Cov[X_2, X_n] \\ \vdots & \vdots & \ddots & \vdots \\ Cov[X_n, X_1] & Cov[X_n, X_2] & \cdots & Var[X_n] \end{pmatrix}$$

It combines the statistical and systematic uncertainties, that are on the diagonal entries and the correlation of the variables in the off-diagonal elements. In the case for the KATRIN measurement they give the uncertainty on the count rate and the correlation between the count rates that were measured at the different retarding potentials.

In **Fitrium** the entries of the covariance matrix are obtained as follows [56]:

1. The values of the parameter  $p$  and its uncertainty  $\sigma_p$  from a prescription or a measurement are used as parameters for a Gaussian distribution with mean  $p$  and width  $\sigma_p$ . From the distribution a number of  $n$  samples is drawn leading to  $n$  different tritium spectra.
2. The  $n$  different tritium spectra are used to estimate the covariance. If a spectrum consists of  $m$  data points the variances and covariance of this data points are estimated which leads to a matrix of dimension  $m \times m$ . A visualization of the matrix can be seen in figure 36.

To perform the fit with the CM, the Gaussian+CM likelihood is chosen in `Fitrium`. If more than one systematic are included the respective covariance matrices are summed to obtain the full covariance matrix containing all systematics.

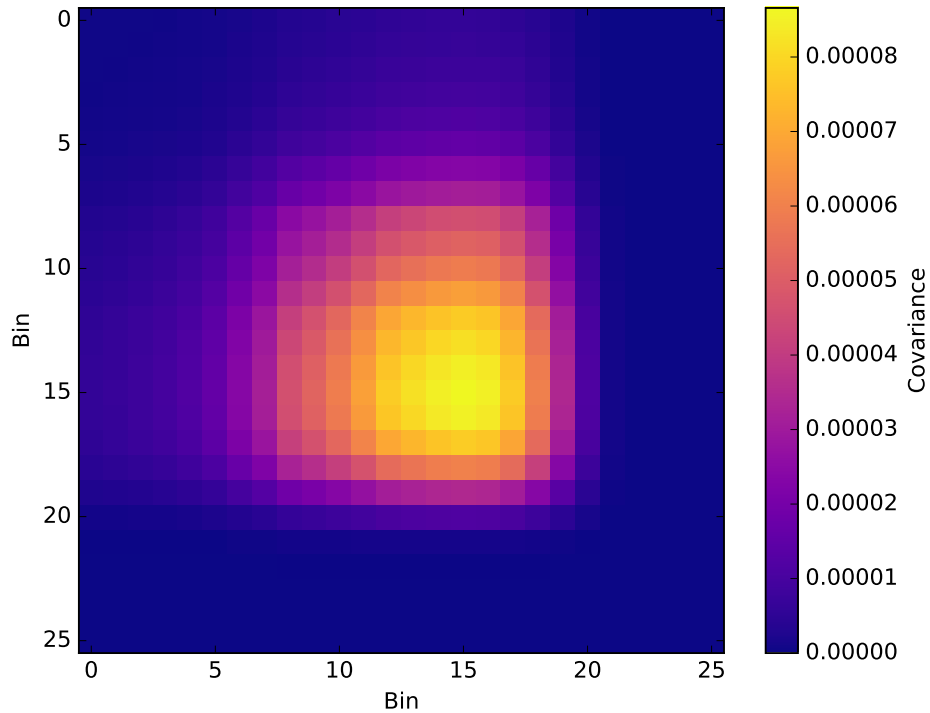


Figure 36: | **Visualisation of Covariance Matrix.** Visualization of the covariance matrix which is obtained by drawing samples from a Gaussian distribution based on a prescription and its uncertainty as described above.

## 8.7 MC-Generation

Before working with real data, the analysis is tested on generated data to show that the fit works. Therefore data was generated to simulate real data with the Monte Carlo generator provided by `Fitrium`. The generated run was based on the same measurement time distribution as was used for the measurements.

The model for the generation includes the same theoretical spectrum and response function as used for the fitting model. The value for the detection efficiency was set to 0.95 and therefore independent of pixels and energy. The active neutrino mass  $m_\beta$  was set to 0, the source parameters are displayed in table 3 and resemble the first tritium settings.

Table 3: | **Model Parameter.** The table displays the values that were used for the model building for the generated data.

quantity	value
Tritium Purity	0.95
Column Density	$4.453 \cdot 10^{21} \frac{\text{molecules}}{\text{m}^2}$
T <sub>2</sub> Fraction	$1.204 \cdot 10^{-4}$
HT Fraction	$4.652 \cdot 10^{-4}$
DT Fraction	$1.039 \cdot 10^{-2}$

Figure 38 shows the result that was obtained by testing the analysis strategy on generated data. The best fit with the full CM has a likelihood of<sup>15</sup>

$$-\ln \mathcal{L}_{min} = 10.053 \Rightarrow \frac{\chi^2}{dof} = \frac{20.106}{23} = 0.874$$

and the spectrum that belongs to this fit can be found in figure 37.

In total five fits were performed. The first fit does not include the CM but only the statistical Poisson distributed uncertainty. The other fits were performed with the Covariance Matrix assuming a Gaussian distribution of the data. For each fit one systematic effect was added. The fit shows that the systematics with the greatest impact are the uncertainty on the column density and the DT fluctuation. In the lower mass region the effect due to the column density is more important whereas in the higher mass region the effect due to the DT fluctuation gives the leading contribution: The DT fluctuation gives an uncorrelated uncertainty. This uncorrelated uncertainty could most easily imitate a kink in the spectrum. DT fluctuations are more important far away from the endpoint as the statistical uncertainty gets smaller for high count rates there. The fit on the generated data shows that the analysis strategy should work if the underlying model that was used for generation of the data is in agreement with real data (see figure 38). A pixel and energy dependent detection efficiency was not included for data generation and fitting model. This is done in the next section when considering real data.

---

<sup>15</sup>The fit included 26 data points and optimized the model according to 3 fitting parameters which leads to 23 degrees of freedom.

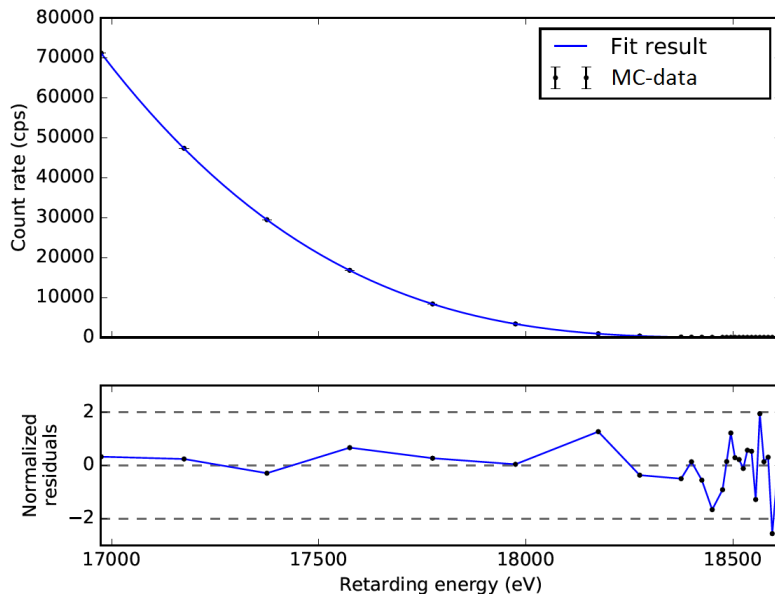


Figure 37: | **Fit Result from Generated Data.** The figure shows the spectrum resulting from the best fit with generated data and the corresponding normalized residuals.

## 8.8 Results from Real Data

After the analysis strategy has been approved with generated data, it is applied to real data. The only difference is that, for the exclusion curve based on the real data, the pixel and energy dependent detection efficiency is included instead of assuming a constant detection efficiency. In total five fits were performed. The first fit did not include systematics and was only based on the Poisson distributed statistical uncertainty (blue exclusion line). All other fits include the CM and are assuming a Gaussian distribution of the data. For each new scan a systematic effect was added. The best fit value of the final exclusion curve that takes into account all effects is

$$-\ln \mathcal{L}_{min} = 5.814 \Rightarrow \frac{\chi^2}{dof} = 0.506$$

The spectrum resulting from this fit is shown in figure 40. The figure shows that the main contributions are the column density (green exclusion line) and the DT fluctuation (purple exclusion line). The magnetic fields and the onset of FSD have only minor effects on the fit result. This corresponds to the observations from the generated data. The exclusion plot shows that a good understanding of the systematics is of utmost importance. Including all systematics will not only shift up the exclusion curve, but can also change the result profoundly. Whereas for example the scan taking into account only statistics sees a sterile neutrino signal, the scan including all mentioned systematics can only set an exclusion limit. Fits with underestimated systematics lead to a larger difference of the logarithmic likelihoods compared to the fits resulting from a correct treatment of systematics. This can lead to a falsely detected sterile neutrino signal.

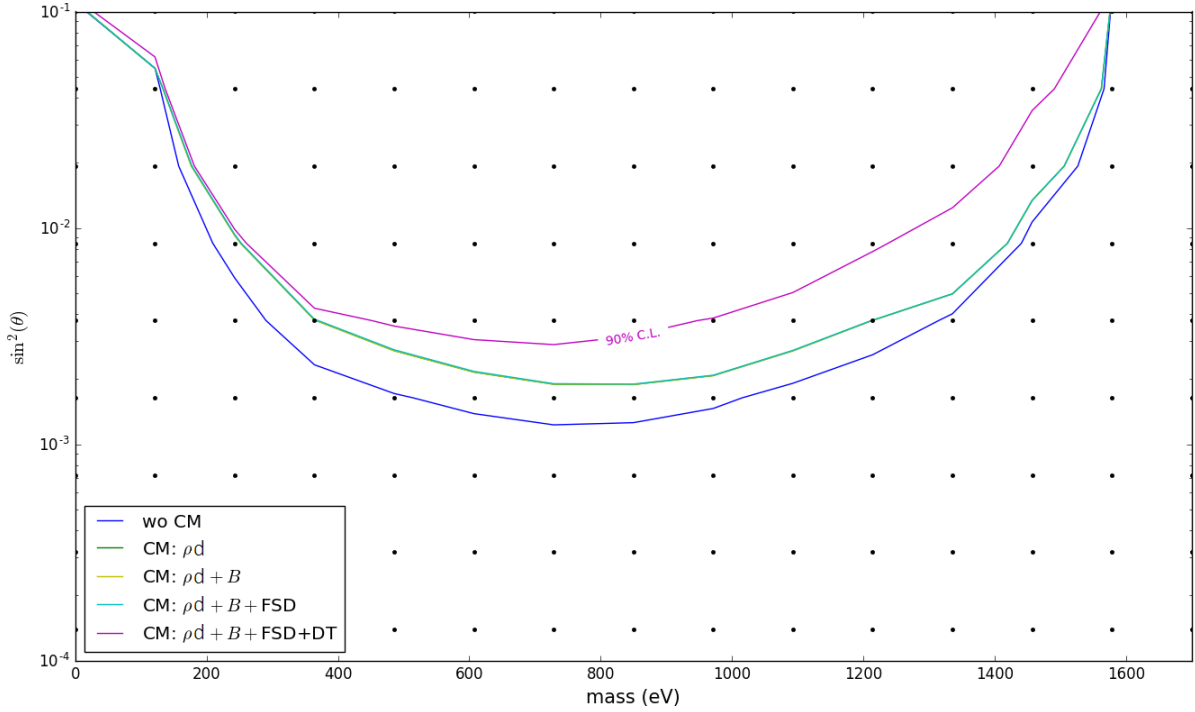


Figure 38: | **Exclusion Curve Based on Generated Data.** To validate the fit and the results obtained with the real data, the same analysis was performed on generated data. The figure shows the 90% exclusion curve for data based on the first tritium configurations. The systematics that are mainly contributing to the improvement of the fit are the uncertainty on the column density  $\rho d$ , and the DT-fluctuation. The uncertainty on the magnetic field and the FSD onset, do not give a noticeable improvement on the fit. The plot confirms that the analysis works on generated data. The generated data and the model do not include a pixel and energy dependent detection efficiency.

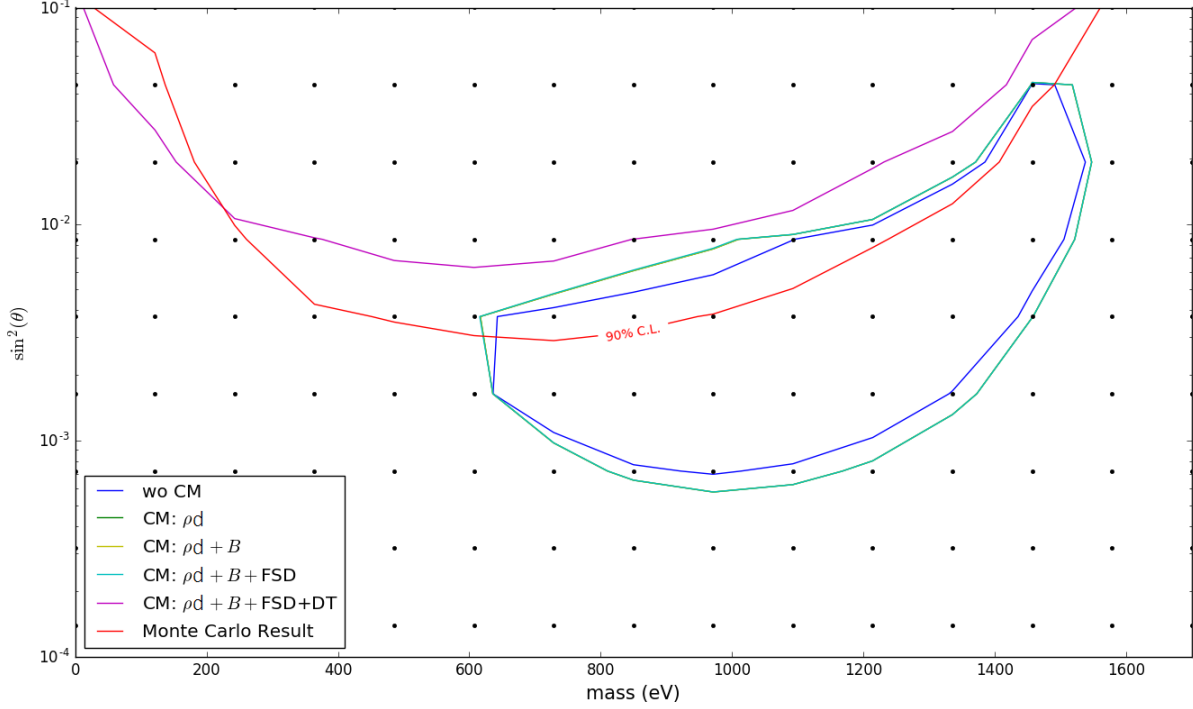


Figure 39: | **Final Exclusion with Fitrium.** The figure shows the final exclusion curve with 90% C.L. obtained from one 3-hour run, that was measured during the FT measurement. The main changes of the fit results are due to uncertainties of the column density (green exclusion line) and the DT fluctuation (purple exclusion line). The uncertainty on the magnetic fields that includes the maximal magnetic field and the fields in the analysing plane and the source do not have a large impact on the fit and neither does the onset of the FSD. The plot shows that the systematics can change the fit result drastically. The DT fluctuation changes the scan result from an island that would denote a sterile neutrino signal into an exclusion curve. A good understanding of the systematics is of high importance.

### 8.8.1 qU-scans

For a stable fit the fit parameters should not vary when choosing a different fitting range. In order to prove the stability of the fit and make the exclusion plot reliable a qU-scan was performed. The data from run 40667 was fitted once with and once without CM. The sterile parameters used in the fit model were  $m_4 = 0$  keV and  $\sin^2 \theta_S = 10^{-8}$ . Figure 41 shows the fit results from a fit with CM and without CM. The y-axis displays the difference of the fitted endpoint value to 18575 eV, the x-axis shows the lower limits of the fitting ranges, the upper limit is the same for all fits and is the maximal retarding potential that was measured. Without CM the uncertainties are only due to statistics and increase towards small fitting ranges that contain only low count rates. The inclusion of the CM results in a fit makes it more stable in the sense that it is independent from the lower

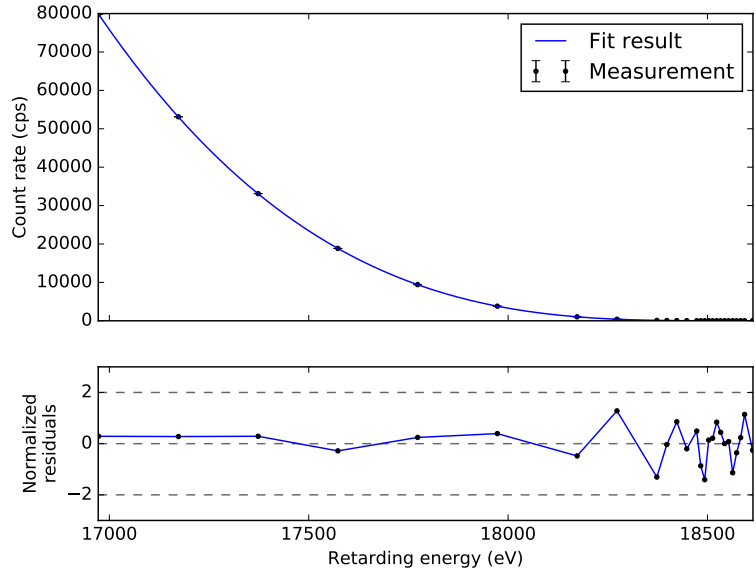


Figure 40: | **Fit Result from Real Data.** The figure shows the spectrum resulting from the best fit for the real data and the corresponding normalized residuals.

limit of the fitting range. The fluctuations are all within the uncertainties. The scan confirms the reliability of the fit results.

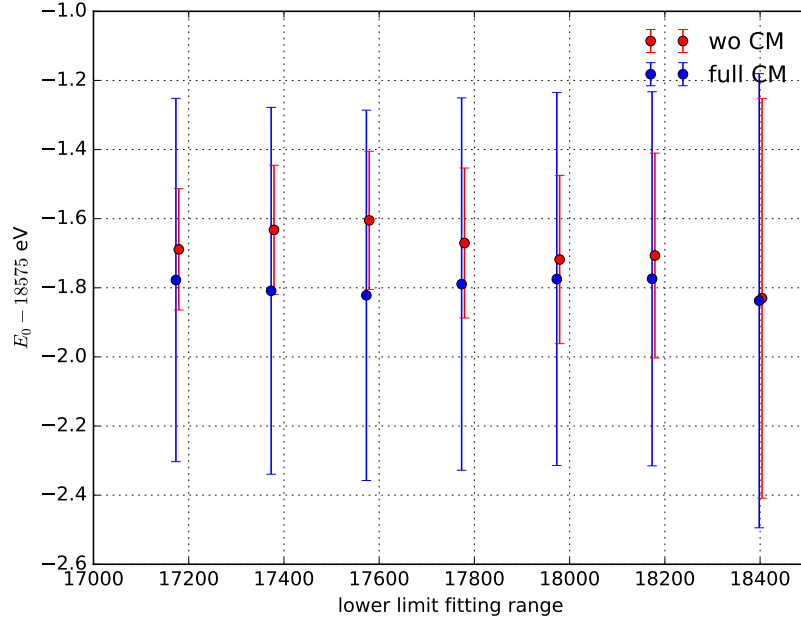


Figure 41: |  $qU$ -scan. The figure shows the stability of the fit when considering the systematics with the CM approach. The y-axis displays the fitted endpoint value relative to 18575 eV, the x-axis displays the lower limit of the fitting range. The upper limit is the data point taken at the highest retarding potential and the same for all fits. Without CM the uncertainties are only due to statistics and therefore increase towards smaller fitting ranges. The stability of the fit is improved when taking into account the CM. The data points of the  $qU$ -scan without CM is slightly shifted for better comparison.

### 8.8.2 Comparison to Exclusion Lines from Other Runs

The exclusion curve is based on a single run, namely run 40667. To classify the exclusion curve obtained for this runs into the ones obtained from other runs, multiple scans for all 3-hour-runs of the tritium measurements were performed with the CM including all systematics. Figure 42 contains the exclusion lines of all runs. Only single runs show larger deviances from the result of run 40667. The differences could result from fluctuations in the data.

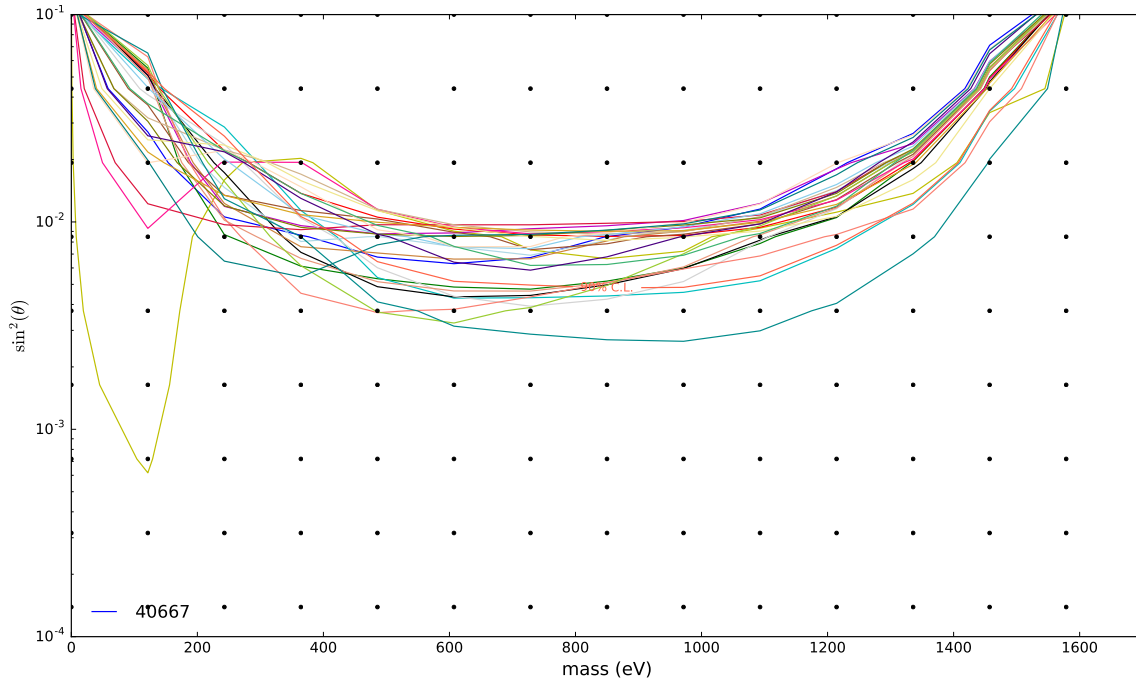


Figure 42: | **Exclusion Lines from All Runs.** The figure shows the final exclusion curve with 90% C.L. obtained from all 3-hour runs, that was measured during the FT measurement. The runs give similar results for the exclusion limit. The run number 40667 that was mainly used in this thesis leads to the blue exclusion line.

### 8.8.3 Results from Other Experiments

Figure 43 shows the exclusion lines obtained by various experiments. The result obtained with this analysis is also included (purple exclusion line). Although the data analysis was based only on data taken in 3-hours, it is already able to give a slight improvement on the exclusion in the keV region.

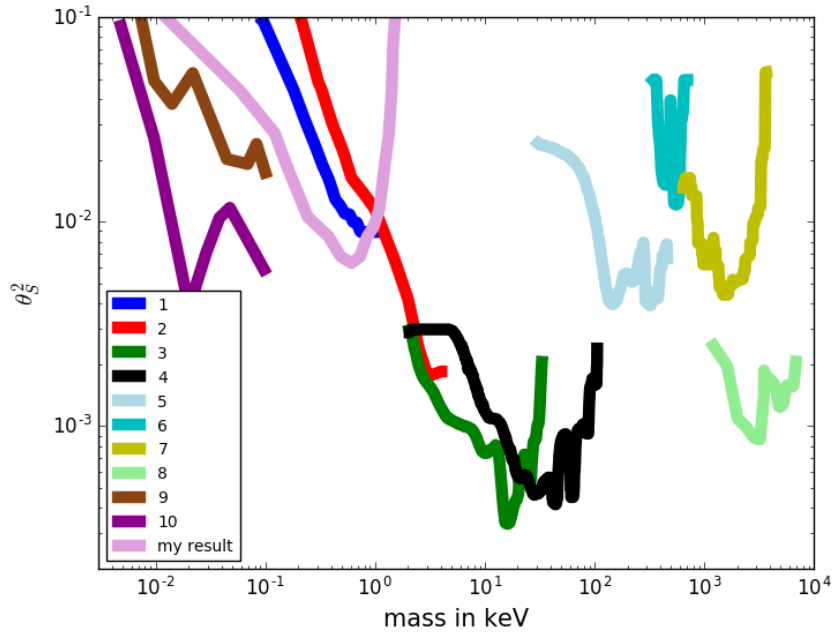


Figure 43: | **Exclusion Lines from Various Experiments.** The figure shows the exclusion lines obtained in various experiments. The final result of this thesis is based on a 3-hour run taken in the FT measurements. Exclusion lines are from 1:  $\beta$ -decay of  $^{187}\text{Re}$  [57], 2: tritium  $\beta$ -decay [58], 3:  $\beta$ -decay of  $^{63}\text{Ni}$  [59], 4:  $\beta$ -decay of  $^{35}\text{S}$  [60], 5:  $^{64}\text{Cu}$  decay [61], 6: recoil spectra of  $^{37}\text{Ar}$  decay [62], 7: Decay of  $^{38\text{m}}\text{K}$  [63], 8:  $\beta$ -spectrum of  $^{20}\text{F}$  [64], 9: tritium  $\beta$ -decay [65], 10: tritium  $\beta$ -decay [66].

## 9 Conclusion and Outlook

An analysis of the first tritium data has been performed with `Fitrium`. It was based on a single 3-hour run that covered an energy range down to 1.6 keV below the endpoint and resulted into an exclusion limit (90% C.L.) in a mass range of 0.5 - 1.6 keV. The relevant systematic uncertainties have been taken into account with the so-called Covariance Matrix approach. The analysis shows that the dominant uncertainties in this First Tritium measurement campaign are the uncorrelated DT fluctuations and the column density. Moreover it has been shown that the systematic effects have to be understood very well as an underestimation could change the result of sterile neutrino analysis.

In order to search for the potential characteristic signature of a keV-scale sterile neutrino in  $\beta$ -decays, the entire spectrum has to be measured with high precision.

While the model provided by `Fitrium` (optimized for neutrino mass measurements) was sufficient, forthcoming sterile neutrino searches with KATRIN, will require a more detailed model that includes effects that become relevant further from the endpoint, such as multiple scatterings and backscattering from the detector surface.

In this work a new software package, called SSC-sterile was presented. In SSC-sterile relevant physics effects are described in the form of response matrices, that describe how the effect alters the energy and angular distribution of  $\beta$ -electrons. The response matrix due to backscattering on the detector as a function of the retarding potential was investigated and the corresponding matrices were computed as an input for SSC-sterile.

The analysis can also be extended by using several combinations of runs and pixels, like multi-pixel fits and stacking or appending of runs.

Nevertheless the results obtained in this thesis are already able to compete with results from other neutrino experiments.

## Acknowledgements

This thesis was not only the result of my own work, but also of the help I got from many other persons along the way. Therefore I would like to thank

- Prof. Dr. Susanne Mertens, for giving me the possibility to write this thesis in her group and for being an inspiration to me with her way of being a leader.
- Martin Slezák and Christian Karl, for providing the Fitrium software and for always solving problems within minutes when I needed help or had any technical issues.
- Alexey Lokhov, for explaining the SSC-sterile software to me and for his kind and attentive support during the time in Munich and Karlsruhe.
- Anton Huber and Leonard Köllenberger, for helping me when I had questions and for filling the time we had together with good mood.
- the members of the container ground floor, for including me in all the adventures at and away from work.
- Pablo, por darme la libertad que necesité y por rellenar mi vida.
- meiner Familie, dafür, dass ihr mich immer in allem unterstützt, was ich mache.

## List of Figures

1	$\beta$ -Decay Spectrum . . . . .	2
2	Fermi Diagram $\beta$ -decay . . . . .	2
3	Detection Principle Anti-Neutrino . . . . .	4
4	The Savannah River Experiment . . . . .	5
5	Set-Up KATRIN Experiment . . . . .	12
6	The $\beta$ -Decay Spectrum . . . . .	14
7	Rear Section . . . . .	15
8	WGTS . . . . .	16
9	DPS . . . . .	17
10	CPS . . . . .	17
11	Main Spectrometer . . . . .	19
12	Principle of MAC-E Filter . . . . .	20
13	Focal Plane Detector . . . . .	21
14	KATRIN Pixel Detector . . . . .	22
15	KATRIN Response Function . . . . .	23
16	Tritium Spectrum with Sterile Neutrino . . . . .	25
17	Prototypes of Pixel Detector for Phase 1 of the TRISTAN project . . . . .	27
18	Terminology in KASSIOPEIA . . . . .	28
19	Initialisation of Particle Simulation with Kassiopeia . . . . .	29
20	Field Configurations . . . . .	30
22	Exact and Adiabatic Trajectories . . . . .	32
21	KASSIOPEIA Simulations . . . . .	32
23	Transformation of Monoenergetic Particles . . . . .	36
24	Transformation of Spectrum . . . . .	37
25	Response Matrix . . . . .	38
26	Response Matrices . . . . .	41
27	Backscattering in Detector . . . . .	42
28	Detector Responses . . . . .	43
29	Retarding Potential Dependence . . . . .	44
30	Detection Efficiency . . . . .	45
31	Backscattering Spectra . . . . .	46
32	Final Energy Deposition . . . . .	46
33	Measurement Time Distribution (MTD) . . . . .	48
34	Pixel Non-Uniformity . . . . .	50
35	Pile-Up loss . . . . .	51
36	Visualisation of Covariance Matrix . . . . .	54
37	Fit Result from Generated Data . . . . .	56
38	Exclusion Curve Based on Generated Data . . . . .	57
39	Final Exclusion with Fitrium . . . . .	58
40	Fit Result from Real Data . . . . .	59
41	$qU$ -scan . . . . .	60
42	Exclusion Lines from All Runs . . . . .	61
43	Exclusion Lines from Various Experiments . . . . .	62

**List of Tables**

1	Oscillation Parameters . . . . .	8
2	Configuration for First Tritium . . . . .	47
3	Model Parameter . . . . .	55

## References

- [1] K. Eguchi et al. “First Results from KamLAND: Evidence for Reactor Antineutrino Disappearance”. *Physical Review Letters* 90.2 (2003). DOI: 10.1103/PhysRevLett.90.021802.
- [2] Q. R. Ahmad et al. “Direct Evidence for Neutrino Flavor Transformation from Neutral-Current Interactions in the Sudbury Neutrino Observatory”. *Physical Review Letters* 89.1 (2002). DOI: 10.1103/PhysRevLett.89.011301.
- [3] R. Mößbauer. “History of Neutrino Physics: Pauli’s Letters” (1998).
- [4] E. Fermi. “Versuch einer Theorie der beta-Strahlen”. *Zeitschrift für Physik* 88.3 (1934). DOI: 10.1007/BF01351864.
- [5] F. A. Scott. “Energy spectrum of the  $\beta$ -rays of radium E”. *Physical Review* 48.5 (1935). DOI: 10.1103/PhysRev.48.391.
- [6] “The Reines-Cowan Experiments”. *Los Alamos Science* 25 (1997). URL: <https://permalink.lanl.gov/object/tr?what=info:lanl-repo/lareport/LA-UR-97-2534-02>.
- [7] G. Danby et al. “Observation of High-Energy Neutrino Reactions and the Existence of Two Kinds of Neutrinos”. *Physical Review Letters* 9.1 (1962). URL: <https://link.aps.org/doi/10.1103/PhysRevLett.9.36>.
- [8] K. Kodama et al. “Observation of tau neutrino interactions”. *Physics Letters B* 504.3 (2001). DOI: [https://doi.org/10.1016/S0370-2693\(01\)00307-0](https://doi.org/10.1016/S0370-2693(01)00307-0). URL: <http://www.sciencedirect.com/science/article/pii/S0370269301003070>.
- [9] R. Davis. “A review of the homestake solar neutrino experiment”. *Progress in Particle and Nuclear Physics* 32 (1994). DOI: [https://doi.org/10.1016/0146-6410\(94\)90004-3](https://doi.org/10.1016/0146-6410(94)90004-3). URL: <http://www.sciencedirect.com/science/article/pii/0146641094900043>.
- [10] K. Nakamura, U. Tokyo, and S. Petcov. “Neutrino Masses, Mixing, and Oscillations”. *The Review of Particle Physics* (2017).
- [11] T. Katori and Q. Mary. “Search for Electron Antineutrino Appearance at the  $\Delta m_{21}$  eV Scale” (2014).
- [12] T. Lasserre. “The reactor antineutrino anomaly”. *Proceedings of Science* (2011). DOI: 10.1088/1742-6596/408/1/012025.
- [13] C. Giunti and C. W. Kim. “Fundamentals of Neutrino Physics and Astrophysics” (2007).
- [14] R. D. Klauber. *The Seesaw Mechanism*. URL: <http://www.quantumfieldtheory.info/TheSeesawMechanism.htm> (visited on 11/19/2018).
- [15] M. Spinrath. *Gibt es noch Neutrinos?* URL: <https://web.physik.rwth-aachen.de/%7B%7Dstahl/Seminar/SpinrathVortrag.pdf> (visited on 11/20/2018).
- [16] R. Adhikari et al. “A white paper on keV sterile neutrino dark matter”. *Journal of Cosmology and Astroparticle Physics* 2017.1 (2017). DOI: 10.1088/1475-7516/2017/01/025.
- [17] C. Karl. “Analysis of First Tritium Data of the KATRIN Experiment” (2018).
- [18] J. Angrik et al. “KATRIN Design Report 2004” (2005).
- [19] C. Kraus et al. “Final results from phase II of the Mainz neutrino mass search in tritium  $\beta$ -decay”. *The European Physical Journal C - Particles and Fields* 40.4 (2005). DOI: 10.1140/epjc/s2005-02139-7. URL: <https://doi.org/10.1140/epjc/s2005-02139-7>.

- [20] V. N. Aseev et al. “Upper limit on the electron antineutrino mass from the Troitsk experiment”. *Phys. Rev. D* 84.11 (2011). DOI: 10.1103/PhysRevD.84.112003. URL: <https://link.aps.org/doi/10.1103/PhysRevD.84.112003>.
- [21] V. N. Aseev et al. “Measurement of the electron antineutrino mass in tritium beta decay in the Troitsk  $\nu$ -mass experiment”. *Physics of Atomic Nuclei* 75.4 (2012). DOI: 10.1134/S1063778812030027. URL: <https://doi.org/10.1134/S1063778812030027>.
- [22] M. Kleesiek et al. “ $\beta$ -Decay Spectrum, Response Function and Statistical Model for Neutrino Mass Measurements with the KATRIN Experiment” (2018).
- [23] J. N. Abdurashitov et al. “First measurements in search for keV-sterile neutrino in tritium  $\beta$ -decay by Troitsk  $\nu$ -mass experiment” (2017).
- [24] *KATRIN web page*. URL: <http://www.katrin.kit.edu/768.php> (visited on 09/17/2018).
- [25] M. Sturm. “Aufbau und Test des Inner-Loop-Systems der Tritiumquelle von KATRIN” (2010).
- [26] B. Bornschein et al. “Measurement of the gas-flow reduction factor of the KATRIN DPS2-F differential pumping section” (2018).
- [27] S. Reimer. “Ein elektrostatisches Dipolsystem zur Eliminierung von Ionen in der DPS2-F des KATRIN Experimentes” (2009). URL: <http://www.katrin.kit.edu/publikationen/dth-reimer.pdf>.
- [28] S. Groh. “Modeling of the Response Function and Measurement of Transmission Properties of the KATRIN Experiment” (2015).
- [29] W. Gil et al. “The Cryogenic Pumping Section of the KATRIN Experiment”. *IEEE Transactions on Applied Superconductivity* 20.3 (2010). DOI: 10.1109/TASC.2009.2038581.
- [30] S. Gäthke. “Transport mit Umwegen” (2006). URL: [https://www.deutschlandfunk.de/transport-mit-umwegen.676.de.html?dram:article%7B%5C\\_%7Did=23967](https://www.deutschlandfunk.de/transport-mit-umwegen.676.de.html?dram:article%7B%5C_%7Did=23967).
- [31] N. Wandkowsky. “Study of background and transmission properties of the KATRIN spectrometers” (2013).
- [32] P. I. Morales Guzmán. “Simulation, Data Challenge, and Analysis of First KATRIN Tritium Data” (2018).
- [33] L. Kippenbrock. “Investigation of the FPD Energy Resolution” (2018).
- [34] B. L. Wall et al. “Dead layer on silicon p-i-n diode charged-particle detectors”. *Nuclear Instruments and Methods in Physics Research, Section A: Accelerators, Spectrometers, Detectors and Associated Equipment* 744 (2014). DOI: 10.1016/j.nima.2013.12.048. URL: <http://dx.doi.org/10.1016/j.nima.2013.12.048>.
- [35] V. N. Aseev et al. “Energy loss of 18 keV electrons in gaseous T and quench condensed D films”. *The European Physical Journal D - Atomic, Molecular, Optical and Plasma Physics* 10.1 (2000). DOI: 10.1007/s100530050525. URL: <https://doi.org/10.1007/s100530050525>.
- [36] D. N. Abdurashitov et al. “Electron scattering on hydrogen and deuterium molecules at 14–25 keV by the “Troitsk nu-mass” experiment”. *Physics of Particles and Nuclei Letters* 14.6 (2017). DOI: 10.1134/S1547477117060024.
- [37] P. I. Morales Guzmán. “Simulation, Data Challenge, and Analysis of First KATRIN Tritium Data (Master Thesis Colloquium)”. 2018.

- [38] A. Alborini et al. “Characterization of a prototype silicon drift detector system for the TRISTAN project” (2018).
- [39] M. Korzeczek. “eV- & keV-sterile neutrino studies with KATRIN” (2016).
- [40] F. Roccati. “Novel simulation techniques for a sterile neutrino search with KATRIN” (2018).
- [41] M. Slezák. “Monitoring of the energy scale in the KATRIN neutrino experiment” (2015).
- [42] *magnetischer Spiegel*. URL: <https://www.spektrum.de/lexikon/physik/magnetischer-spiegel/9330> (visited on 10/28/2018).
- [43] *Web Page Max Planck Institute for Physics*. URL: <https://www.mpp.mpg.de/forschung/astro-teilchenphysik-und-kosmologie/katrin-und-tristan-neutrinos-und-dunkle-materie/> (visited on 09/26/2018).
- [44] T. Brunst. “Detector Development for a Sterile Neutrino Search with the KATRIN Experiment”.
- [45] A. A. Esfahani, D. M. Asner, and S. Böser. “Kassiopeia: a modern, extensible C++ particle tracking package”. *New Journal of Physics* 19.5 (2017). DOI: 10.1088/1367-2630/aa6950. URL: <http://dx.doi.org/10.1088/1367-2630/aa6950>.
- [46] D. L. Furse. “Techniques for Direct Neutrino Mass Measurement Utilizing Tritium  $\beta$ -Decay” (2015).
- [47] T. J. Corona. “Tools for Electromagnetic Field Simulation in the KATRIN Experiment” (2009).
- [48] F. Glück. “Axisymmetric electric field calculation with zonal harmonic expansion”. *Progress In Electromagnetics Research B*. 32 (2011). DOI: 10.2528/PIERB11042108.
- [49] A. Lokhov. “SSC validity for the First Tritium measurement” (2018).
- [50] A. Lokhov. “SSC-sterile update” (2018).
- [51] A. Lokhov. “Overall response of RW , source and the spectrometer” (2018).
- [52] C. T. Russell. “Physics of magnetic flux ropes”. *Eos, Transactions American Geophysical Union* 70.26 (1989). DOI: 10.1029/89E000206.
- [53] N. Doss and J. Tennyson. “Excitations to the electronic continuum of  $3\text{HeT}^+$  in investigations of T2  $\beta$ -decay experiments”. *Journal of Physics B: Atomic, Molecular and Optical Physics* 41.12 (2008). DOI: 10.1088/0953-4075/41/12/125701.
- [54] S. Enomoto and M. Korzeczek. “Detection Efficiencies for First Tritium Relative Efficiency” (2018).
- [55] M. Arenz. “First Transmission of electrons and ions through the KATRIN beamline” (2018).
- [56] M. Slezák. *Generating and using covariance matrices with the Fitness Studio / Fitrium software*. URL: <https://nuserv.uni-muenster.de:8443/karlch/Fitrium/blob/master/Docs/CovMatrix.md> (visited on 11/24/2018).
- [57] M. Galeazzi et al. “Limits on the Existence of Heavy Neutrinos in the Range 50 - 1000 eV from the Study of the  $^{187}\text{Re}$  Beta Decay”. *Physical Review Letter* 86 (2001). DOI: 10.1103/PhysRevLett.86.1978. URL: <https://link.aps.org/doi/10.1103/PhysRevLett.86.1978>.
- [58] K. Hiddemann, H. Daniel, and O. Schwentker. *Journal of Physics* 21.639 (1995).

- [59] E. Holzschuh et al. “Search for heavy neutrinos in the  $\beta$ -spectrum of  $^{63}\text{Ni}$ ”. *Physics Letters B* 451.1 (1999). DOI: [https://doi.org/10.1016/S0370-2693\(99\)00200-2](https://doi.org/10.1016/S0370-2693(99)00200-2).
- [60] E. Holzschuh et al. “The  $\beta$ -spectrum of  $^{35}\text{S}$  and search for the admixture of heavy neutrinos”. *Physics Letters B* 482.1 (2000). DOI: [https://doi.org/10.1016/S0370-2693\(00\)00476-7](https://doi.org/10.1016/S0370-2693(00)00476-7).
- [61] K. Schreckenbach, G. Colvin, and F. von Feilitzsch. “Search for mixing of heavy neutrinos in the  $\beta^+$  and  $\beta^-$  spectra of the  $^{64}\text{Cu}$  Decay”. *Physics Letters B* 129.3 (1983). DOI: [https://doi.org/10.1016/0370-2693\(83\)90858-4](https://doi.org/10.1016/0370-2693(83)90858-4).
- [62] M. M. Hindi et al. “Search for the admixture of heavy neutrinos in the recoil spectra of  $^{37}\text{Ar}$  decay”. *Physical Review C* 58 (1998). DOI: 10.1103/PhysRevC.58.2512.
- [63] M. Trinczek et al. “Novel Search for Heavy  $\nu$  Mixing from the  $\beta^+$  Decay of  $^{38\text{m}}\text{K}$  Confined in an Atom Trap”. *Phys. Rev. Lett.* 90 (1 2003), p. 012501. DOI: 10.1103/PhysRevLett.90.012501. URL: <https://link.aps.org/doi/10.1103/PhysRevLett.90.012501>.
- [64] J. Deutsch, M. Lebrun, and R. Prieels. “Searches for admixture of massive neutrinos into the electron flavour”. *Nuclear Physics A* 518.1 (1990). DOI: [https://doi.org/10.1016/0375-9474\(90\)90541-S](https://doi.org/10.1016/0375-9474(90)90541-S).
- [65] C. Kraus et al. “Limit on sterile neutrino contribution from the Mainz Neutrino Mass Experiment”. *European Physics Journal C* 73 (2013).
- [66] A. I. Belesev et al. “A search for an additional neutrino mass eigenstate in 2 to 100 eV region from "Troitsk nu-mass" data” (2012).